Microstructural insights into creep of Ni-based alloy 617 at 700 °C provided by electron microscopy and modelling

Florian Riedlsperger [a,*], Tomasz Wojcik [b], Ricardo Buzolin [c], Gerold Zuderstorfer [a], Magdalena Speicher [d], Christof Sommitsch [c], Bernhard Sonderegger [a]

[a] Institute for Engineering Materials- Metals and Alloys, JKU Linz, 4040 Linz, Austria
[b] Institute of Materials Science and Technology, TU Wien, 1060 Vienna, Austria
[c] Institute of Materials Science, Joining and Forming (IMAT), Graz University of Technology, 8010 Graz, Austria
[d] Materials Testing Institute (MPA), University of Stuttgart, 70569 Stuttgart, Germany

ARTICLE INFO

ABSTRACT

In this work, microstructural changes during creep of Ni-based alloy 617 at 700 °C and 165 MPa have been investigated by electron microscopy, and complementarily modelled. Precipitate types, sizes and chemistry were determined by transmission- (TEM) and scanning electron microscopy (SEM). Apart from γ' particles, MX and carbides, coarse μ-phase was found. Grain size, frequency of twins, deformation patterns and geometrically necessary dislocations were characterized by electron backscatter diffraction (EBSD). Based on measurements and literature data, creep behavior and a time-to-rupture (TTR) diagram of A617 have been numerically simulated at 700 °C in a range of 165 to 215 MPa with a new physical model. Our new creep model achieved excellent agreement with measured data and literature in terms of predicted creep life, times to 1% strain, minimum creep rate and microstructural evolution. We also succeeded in considering the varying ductility of the material in a novel damage law by implementing the reduction of area from fractured creep samples. Diffusion creep (coble creep) is considered in addition to dislocation creep in the model. The impact of diffusion creep is mostly visible at low stresses, leading to significant improvements within the TTR diagram.

1. Introduction

Alloy 617 or A617 (also known as Inconel 617) ranks amongst the solid-solution strengthened Ni-based superalloys [1] and has been developed for high temperature components in thermal power plants and aircraft [2]. High concentrations of Co (11–14 wt%) and Mo (8.5–10 wt%) are contained [2] in these for solid solution purposes. A617 is extremely resistant to both corrosion and (cyclic) oxidation [1–3], because of 20–23 wt% Cr. Further advantages are the good workability and a low coefficient of thermal expansion [3]. Alloy 617B represents a further development of A617 with narrower tolerance windows for the chemical composition and specific information on the B content [3]. A617B exhibits extraordinary creep strength especially between 650 °C and 720 °C [4]. For components of gas-cooled generation IV nuclear reactors, A617 has even been qualified for temperatures up to 950 °C [2]. A617 is also a promising candidate for applications in concentrated solar power [5].

The outstanding creep performance below 750 °C is related to

nucleation of coherent, ordered, evenly distributed, long-term stable γ'precipitates $Ni_3(Al,Ti)$ with lattice type $L1_2$ [6–8]. Unlike other Ni-base alloys, the γ'phase fraction is remarkably smaller than 10% [9,10]. γ'precipitates can be distinctly characterized in TEM by dark field imaging on super-lattice reflections in the electron diffraction patterns [11]. They may under certain conditions change their morphology from spherical to cubic during aging [6,12,13]. The phenomenon seems to be more pronounced and faster for higher creep temperatures [12], longer aging times [6] and larger γ/γ'misfits [13]. Apart from γ'precipitates, inter- and intragranular networks of carbides [4,14] (mainly fcc $M_{23}C_6$ and M_6C [4,11]) as well as fcc Ti-rich MX (carbo-) nitrides [1,9] can be present in A617. A time-temperature-transformation (TTT) diagram and further crystallographic details of all mentioned precipitates are provided by [8].

In Ni-based superalloys, particular attention must be paid to the avoidance of topologically closed-packed (TCP) phases [15]. In A617, detrimental μ-phase [11] (featuring a rhombohedral A_6B_7 crystal structure [15]) has been shown to compete with $M_{23}C_6$ for Cr and Mo

---

[16]. Although high alloying with Mo (> 9 wt%) is beneficial to retard coarsening of γ', the undesired nucleation of coarse μ-phase precipitates may be initiated by this means [16]. Three nucleation mechanisms of μ-phase are stated in literature: a) independent (from the matrix) [17], b) related to metastable TCP σ-phase [17,18] and c) from $M_{23}C_6$ carbides [16]. μ-phase is suspected of fostering grain boundary failure [11]. Its inherent brittleness [17] and the consumption of solid solution strengthening elements from the surrounding matrix [18] lead to associated void and crack nucleation [17].

A617 is prone to formation of annealing twins, i.e., the grains are sub-divided by $\sum 3$ CSL boundaries [19]. However, these twin boundaries have been shown to be rather unfavorable for nucleation of $M_{23}C_6$ which prefer to nucleate on high angle grain boundaries [19]. Dynamic recrystallization upon deformation has been shown to start above 800 °C [20]. Low-angle subgrain boundary formation only takes place in A617 exposed to a stabilizing heat treatment between 950 and 1000 °C [21] or during hot deformation at 950 °C [22], but has not been observed for purely solutionized material [23]. One of the open questions addressed in this paper is the role of twins for the creep mechanism of A617.

During aging, the hardness of A617 has been shown to increase, whereas toughness mostly drops because of $M_{23}C_6$ located at grain boundaries [14]. During creep, crack propagation, damage and failure usually occur along the grain boundaries [4,14], often with supposed involvement of coarse carbides [4]. One of the counter measures for excessive $M_{23}C_6$ coarsening and to support the stabilization of their network is the addition of B [24]. Especially solution heat-treated A617 without additional annealing may experience stress relaxation cracking at 700 °C in case of residual stresses (e.g. induced by welding) [25]. One parameter for monitoring the risk of stress relaxation cracking is the reduction of area, Z, during (slow strain rate) tensile tests, which becomes particularly critical below 10% [25]. Some creep test results for 700 °C suggest that the elongation at rupture and the reachable creep deformation may decrease drastically with smaller applied stresses [10,26,27]. An important factor that additionally impacts both strength and ductility, are segregation phenomena (including B) [3]. S and B are suspected of causing a drop in the elongation at rupture, when concentrations are too high [28].

During creep exposure, the dislocation density of A617 has been observed to increase by around one order of magnitude, from typically around 10^{13} to 10^{14} m^{-2} at 700 °C and intermediate stresses [4,9]. One of the reasons for this rise may be work hardening [10]. Depending on stress and temperature level, three types of interactions between dislocations and γ'precipitates have been proposed [6]: a) shearing (which is also known as cutting), b) Orowan looping and c) local climb.

A constitutive creep model has been proposed by [29] for Ni-based superalloys with a high phase fraction of γ' particles, and applied to Nimonic 90. The model distinguishes gliding from climbing dislocations and implements interparticle distance as well as phase fraction of γ' into the dislocation release rate. The strain rate is assumed to be dominated by climbing instead of gliding dislocations. It has been demonstrated that the minimum creep rate and rupture life of Nimonic 90 may be well predicted by the model.

For Ni-based alloy C263, an important contribution has been made by [30] with a similar concept, involving climbing and gliding dislocations as well as the γ' effect. As a simplification, steady-state creep is assumed which results in the gliding dislocation density rate to be set zero. The model accounts for both annihilation and trapping processes (respectively pinning), so that a simple rate equation for the dislocation

evolution can be created. Also, an attempt is made to consider cutting of γ' precipitates below a critical size by modifying the activation volume in the glide velocity.

For A617, a model for high temperature creep (between 900 and 1000 °C) has recently been introduced by [31,32], taking into account the effect of $M_{23}C_6$ inside the grain and at grain boundaries (with the phenomenon of dislocation pile-ups) as well as grain boundary sliding. However, the model of [31,32] fails at lower temperatures (for instance 700 °C as in this work), since a γ' effect has not been implemented into the concept.

A backstress-based creep model for A617B has been proposed by [21], implementing the strengthening effects of dislocations, carbides and γ'. Dislocation climb and Orowan mechanism are summarized into a phenomenological precipitate backstress equation. Although being convenient and correctly reproducing experimental creep curves, the model requires a high number of fitting parameters, and an explicit evolution of dislocation density is missing.

The aim of this paper is to determine interactions and establish relationships between precipitates, dislocations, matrix boundaries, creep mechanisms and damage. For this purpose, the creep behavior of A617 at 700 °C was modelled, using a physically-based approach, assisted by electron microscopy investigations and accompanied by precipitate calculations.

2. Experimental procedure

2.1. Material

After vacuum-induction melting (VIM) and electro-slag remelting (ESR), the material was forged into ring blocks (outer diameter of 220 mm, inner diameter of 110 mm and height of 150 mm) by company ENPAR.

The chemical composition of A617 is indicated in Table 1. A617 contains at least 20 wt% Cr, 11–14 wt% Co and 8.5–10 wt% Mo. Subsequently, Ni represents only about 60 wt% of the overall chemical composition. The C content of up to 0.1 wt% allows carbides to form, whereas alloying with Ti (0.2–0.6 wt%) and Al (0.7–1.4 wt%) promotes γ'nucleation.

Heat treatment consisted of normalizing (solution heat treatment) at 1150 °C for 1.5 h and water quenching. The manufactured rings were then radially halved and re-joined at company pro-beam AG by electron-beam welding (EBW). Samples were extracted by wire cutting, followed by turning. No post weld heat treatment was performed.

2.2. Creep tests

Creep tests were carried out at 700 °C, applying stresses between 165 and 185 MPa to round M16 samples without fins. The samples had diameters of 9.53, 9.39, 9.25 and 9.00 mm for stresses of 165, 170, 175 and 185 MPa respectively, i.e., smaller diameters were chosen for higher stresses. Rupture times and the reduction of area after failure were documented.

2.3. Thermodynamic calculation and creep simulation

Thermodynamic equilibrium was simulated by MatCalc version 6.03 (rel. 1.000). The database was "mc_ni_v2.034.tdb". For solving the equation system of our creep model, MatLab version 2019a was used.

Table 1
Chemical composition of EN-standardized Alloy 617 [33].

wt.%	Ni	C	Si	Mn	P	S	Cr
A617	bal	0.05–0.1	<0.2	<0.2	<0.01	<0.01	20–23
wt.%	Mo	Co	Cu	Ti	Fe	Al	B
A617	8.5–10	11–14	<0.5	0.2–0.6	<2	0.7–1.4	<0.006

Both MatCalc and MatLab ran on a Windows 10 system with 64 bits and 4 Intel Core 2114 Quad Q9550 @ 2.83 GHz processors.

2.4. Microstructural investigations

Two samples were investigated: a) the base material (BM) before creep (as-received condition) as well as b) gauge and head part of the 700 °C/165 MPa sample which had failed after 34,220 h. The welded zone is beyond the scope of this paper that focuses on the (crept) base material, where the fracture occurred in a distance >1 cm from the

weldment and heat-affected zone. The precipitation state was characterized at TU Wien using transmission electron microscopy (TEM) on a FEI Tecnai F20 device, equipped with a field emission gun and operated at 200 kV acceleration voltage (U_a). TEM samples were ground down to a thickness of approx. 0.1 mm and etched electrochemically on a Struers Tenupol 5, using a 7% perchloric acid solution at 10 V and − 15 °C. Single grains were tilted into the [001] zone axis for bright field and dark field imaging. Since the coherent γ' precipitates are L1$_2$ ordered, dark field imaging on [100] reflections allow their visualization in the disordered face-centered cubic (fcc) γ matrix. Investigation of other

Table 2
Equation framework of a modified dislocation creep model for A617.

Creep model equations and numbering of subterms	Eq.	Ref.
Creep strain rate (modified Orowan equation) $\frac{d\varepsilon}{dt} = \frac{b \bullet \rho_m \bullet v_{eff}}{M \bullet (1 - D_{ppt}) \bullet (1 - D_{cav})}$	(1)	[36,40]
Mobile dislocation density rate $\frac{d\rho_m}{dt} = \underbrace{v_{eff} \bullet \rho_m^{3/2}}_{a} + \underbrace{\frac{\beta \bullet \rho_s \bullet R_{gb}}{h_b^2} \bullet v_{eff}}_{b} - \underbrace{\frac{v_{eff}}{2 \bullet R_{gb}} \bullet \rho_m}_{c} - \underbrace{\frac{v_{eff}}{2 \bullet h_b} \bullet \rho_m}_{c-obst} - \underbrace{8 \bullet \rho_m^{3/2} \bullet v_c}_{d1} - \underbrace{\delta_{anh} \bullet (\rho_m + \rho_s) \bullet \rho_m \bullet v_{eff}}_{e1}$	(2)	[36,37]
Static dislocation density rate $\frac{d\rho_s}{dt} = \underbrace{\frac{v_{eff}}{2 \bullet R_{gb}} \bullet \rho_m}_{c} + \underbrace{\frac{v_{eff}}{2 \bullet h_b} \bullet \rho_m}_{c-obst} - \underbrace{8 \bullet \frac{v_c}{h_b} \bullet \rho_s}_{d2} - \underbrace{\delta_{anh} \bullet \rho_s \bullet \rho_m \bullet v_{eff}}_{e2}$	(3)	[36,37]
Mean obstacle spacing $h_b = 1 / \left(\frac{\sqrt{\rho_m + \rho_s}}{0.8} + \frac{1}{\lambda} \right)$	(4)	New
Individual interparticle spacing of γ' and M$_{23}$C$_6$ $\lambda_i = \sqrt{\frac{\ln(3)}{2\pi N_v r} + \frac{8}{3} r^2} - \sqrt{\frac{8}{3}} r$	(5.1)	
Total interparticle spacing of all grain-interior precipitates $\lambda = \sqrt{\frac{\ln(3)}{2\pi \sum_i (N_{V,i} r_i)} + (2 r_A)^2} - 2 r_A$ $r_A = \sqrt{\frac{2}{3}} \bullet \frac{\sum_i (N_{V,i} r_i^2)}{\sum_i (N_{V,i} r_i)}$	(5.2)	[41]
Effective velocity $\frac{1}{v_{eff}} = \frac{1}{v_g} + \sum_i \frac{\pi}{2} \bullet N_{V,i} \bullet r_i^3 \bullet \frac{1}{v_c}$	(6)	[36]
Dislocation glide velocity $v_g = a_1 \bullet exp\left\{ -\frac{Q}{k_B \bullet T} \right\} \bullet exp\left\{ -\frac{\sigma_i \bullet V_r}{k_B \bullet T} \right\} \bullet 2 \bullet sinh\left\{ \frac{\sigma_{app} \bullet V_r}{k_B \bullet T} \right\}$	(7)	[36]
Dislocation climb velocity $v_c = v_{cl} + v_{cp}$	(8)	[37]
Dislocation climb velocity- lattice diffusion share $v_{cl} = \frac{2 \bullet \pi \bullet \eta_v \bullet D_s}{\left[1 - \eta_v \bullet \ln\left(L_a \bullet \sqrt{\rho_t} \right) \right] \bullet b} \bullet exp\left\{ -\frac{\sigma_i \bullet \Omega}{k_B \bullet T} \right\} \bullet 2 \bullet sinh\left\{ \frac{\sigma_{app} \bullet \Omega}{k_B \bullet T} \right\}$	(8.1)	[36]
Dislocation climb velocity- pipe diffusion share $v_{cp} = \frac{2 \bullet \pi \bullet b \bullet D_{vp}}{L_p^2} \bullet exp\left\{ -\frac{\sigma_i \bullet \Omega}{k_B \bullet T} \right\} \bullet 2 \bullet sinh\left\{ \frac{\sigma_{app} \bullet \Omega}{k_B \bullet T} \right\}$	(8.2)	[36]
Internal stress $\sigma_i = \alpha \bullet M \bullet G \bullet b \bullet \sqrt{\rho_m + c_s \bullet \rho_s}$	(9)	[39,42]
Damage rate due to cavities $\dot{D}_{cav} = \underbrace{(1/Z)}_{A} \bullet \dot{\varepsilon}$	(10)	New
Overall damage caused by precipitate coarsening of GB particles $D_{ppt} = 1 - \prod_{i=1}^{n} (1 - D_{ppt,i})$	(11)	[36]
Damage rate caused by precipitate coarsening $\dot{D}_{ppt,i} = \frac{k_p}{l_{GB} - 1} \bullet (1 - D_{ppt,i})^{l_{GB}}$	(11.1)	[43]
Normalized Ostwald ripening parameter $k_p = \frac{k_d}{r_{i,0}^3} = \left[\frac{r_i^3(t)}{r_{i,0}^3} - 1 \right] \bullet t^{-1}$	(11.1.1)	[39]
Ostwald ripening parameter $k_d = \frac{r_i^3 - r_{i,0}^3}{t}$	(11.1.1.1)	[44]

Table 3

Overview of input parameters for the creep model from literature and measurements.

Parameters from literature			
Input	Value	Material (group)	Source
a_g	$3.59 \cdot 10^{-10}$ m	Ni- fcc	[45]
β	0.0375	Model specific value	[36]
b	$2.54 \cdot 10^{-10}$ m	Ni- fcc	[45]
c_s	0.3		[39]
δ_{anh}	$6 \cdot 10^{-9}$ m	Ni- fcc (750 K)	[46]
D_s	$9.0 \cdot 10^{-20}$ m^2/s	Ni- fcc (bulk diffus. 700 °C)	[47]
E_{pipe}	4.03–$5.52 \cdot 10^{-19}$ J	A617 (700 °C)	[48–50]
η_v	10^{-5}	Estimation for $\Gamma = 0.1$ J/m^2 [45]	[37]
G	64 GPa	A617 (700 °C)	[51]
l_{GB}	4	Parameter for grain boundary (GB) particle coarsening	[36]
k_B	$1.38065 \cdot 10^{-23}$ J/K	Fundamental constant	[52]
M	3	Crystals (approximation)	[39]
Q	$1 \cdot 10^{-19}$ to $5 \cdot 10^{-19}$ J	Ni- fcc	[30] [53]
V_r	$100 \cdot b^3$ to $263 \cdot b^3$ See Table 8; see Section 5.5.4	Alloy C263 Coarse-grained Ni Ni deformed at high stress Ni with grain size 500 µm	[30] [54] [54] [55]
ν	0.3	A617	[51]

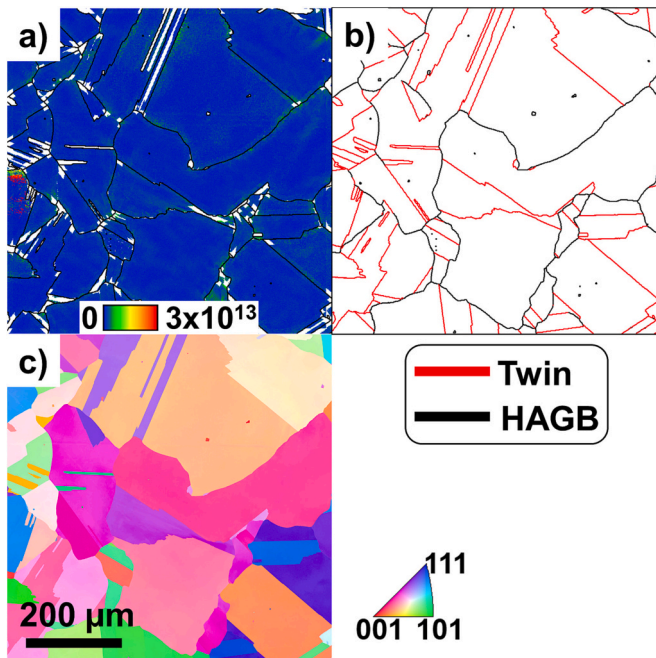| Microstructural input parameters (start values)			
Input	Value	Material (group)	Source
$\rho_{m,0}$	$4 \cdot 10^{13}$ m^{-2}	A617 as-rec. Cond. (BM)	TEM (this work)
$\rho_{s,0}$	$4 \cdot 10^{12}$ m^{-2}	A617 as-rec. Cond. (BM)	10% of $\rho_{m,0}$ [39]
R_{gb}	250 µm	A617 as-rec. Cond. (BM)	EBSD (this work)

Fig. 1. EBSD of BM (as-rec.) showing a) GND map (with white areas out of the range), b) twins and HAGBs, c) misorientations in the IPF map.

phases was performed using selected area electron diffraction (SAED) and energy dispersive X-ray spectroscopy (EDX) in scanning TEM mode (STEM), using a high angle annular dark field (HAADF) detector for mass contrast. Dislocation densities were estimated by a mean-linear intercept method applied to TEM images, as stated in [34]. Dislocations were observed and analyzed both in [001] zone axis and in a two-
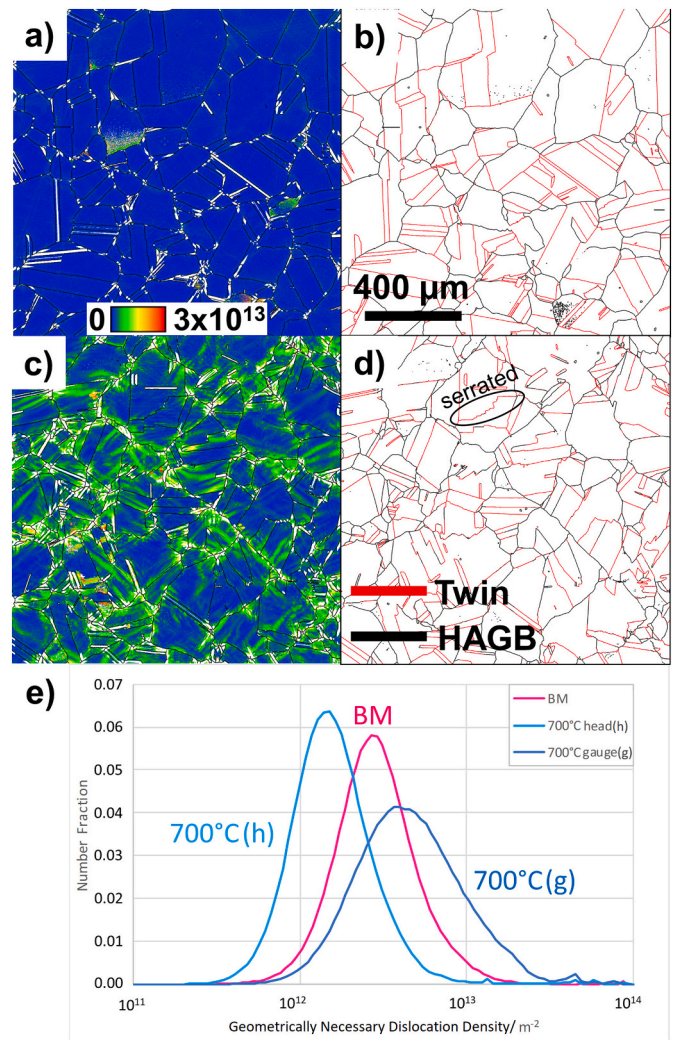

Fig. 2. EBSD after 34,220 h of creep at 700 °C/165 MPa portraying a) GNDs in the head (white areas out of range), b) twins and HAGBs in the head, c) GNDs in the gauge (white areas out of range), d) twins and HAGBs in the gauge, e) distribution of GND density in BM (as-rec. condition) as well as gauge (g) and head (h) section of the crept sample after 34,220 h at 700 °C/165 MPa.

beam condition. The TEM sample thickness was estimated with a log-ratio technique, using an electron energy loss spectrum (EELS), see e. g. [35]. Grain type, grain size, misorientations and geometrically necessary dislocations (GND) were determined by electron back-scattered diffraction (EBSD) at TU Graz. Cavities and large precipitates were also detected at TU Graz by scanning electron microscopy (SEM). SEM analysis was conducted using a Tescan Mira3 microscope equipped with a Hikari EBSD camera and an EDX detector. Secondary electron (SE) and backscattered electrons (BSE) images were acquired using $U_a = 10$ to 25 kV, together with a working distance (WD) of 10 to 15 mm and a spot size (SS) of 4 to 30 nm. Chemical elemental analysis was carried out using $U_a = 15$ to 20 kV, WD = 15 mm and SS = 20 to 40 nm. A setting of $U_a = 30$ kV, WD = 15 to 30 mm and SS = 40 to 100 nm was applied for EBSD measurements which were processed by an APEX® software package. Data were post processed and evaluated by software OIM DataAnalysis® v8.6. A confidence index (CI) standardization was performed, considering a minimum grain size of 5 points and a minimum boundary misorientation angle of 15°. Finally, a neighboring CI correlation was used to re-index the data-points with a CI lower than 0.3. The GND density was calculated by OIM, considering the possible slip systems for a fcc system: $\{111\}\langle 1\bar{1}0\rangle$.

3. Creep model description

In this work, we modify a recently published mean-field dislocation creep model [36] and adapt it to the microstructural constituents present in A617 by following modifications. Contrary to the original model as presented in [36], we do not consider low-angle subgrain boundaries here, since they are not present in the solution-treated material [23]. Subsequently, only mobile (ρ_m) and static dislocation density (ρ_s) evolve and need to be considered in a system of rate equations that accounts for various microstructural interactions. The final aim is to calculate the creep strain rate from Orowan's law, see eq. (1). We replace terms that formerly contained the subgrain radius R_{sgb} in [36] by terms using the grain radius R_{gb} (equal to half the grain size). This applies to the emission of statics (b) and the immobilization term (c) in [36]. Moreover, we introduce an additional immobilization term (c-obst, see eq. 2 and 3) which contains a new formulation of the mean obstacle spacing, h_b. h_b combines the spacing of mobile and static dislocations with the interparticle distance of grain-interior precipitates, λ, see eq. (4). λ sums up individual contributions from γ' and $M_{23}C_6$ particles which are located inside grains, see eq. (5.1) and (5.2). Consequently, the new term (c-obst) reflects the ability of precipitates and/or the creation of a dislocation network [30] to impede the motion of mobile dislocations.

Glide, climb and effective velocity, as also the internal stress remain the same as suggested in [36], see eq. (6) to (9). For calculation of the glide velocity v_g, activation energy Q and activation volume V_r are required. For the lattice diffusion part of the climb velocity v_{cl}, the parameter L_α needs to be determined, depending on shear modulus G, Poisson's ratio ν and Burgers vector b [36]. v_{cl} also contains the important transfer number of defects into jogs η_v, which is related to the stacking fault energy Γ of a material [37]. Details on how to calculate parameter L_p for the pipe diffusion part of the climb velocity v_{cp} based on jog energies (once more a function of G, b and ν) are given in [36]. Apart from the use of λ in the rate equations, the effective velocity v_{eff} represents an additional instrument of taking into account possible interactions of dislocations with precipitates. v_{eff} quantifies climb over particles [36].

The model for cavitation damage (parameter D_{cav}) is inspired by [38], see eq. (10). As a difference, we use the inverse of the reduction of area, $1/Z$, as a damage pre-factor (formerly A) which accounts for the level of ductility in the material and affects reachable strain and lifetime. Cavitation damage reflects damage to due void/ cavity formation in the course of creep [38], which is especially relevant in the tertiary stage of creep. Precipitate damage (parameter D_{ppt}) is used identically to [36], see eq. (11). However, in this case, the concept is only applied to grain boundary precipitates (namely $M_{23}C_6$ and μ-phase). As stated by [39], precipitate damage is caused by excessive coarsening of precipitates combined with solid solution depletion.

Once the evolution of mobile dislocation density ρ_m is known (from solving the differential equation system) and the effective velocity v_{eff} has been determined, the creep strain based on a modified Orowan law with damage parameters can be calculated, as stated in eq. (1).

100% of damage for either D_{ppt} or D_{cav} serve as failure criterion and end the calculation.

An overview on all equations of the modified dislocation creep model is given in Table 2.
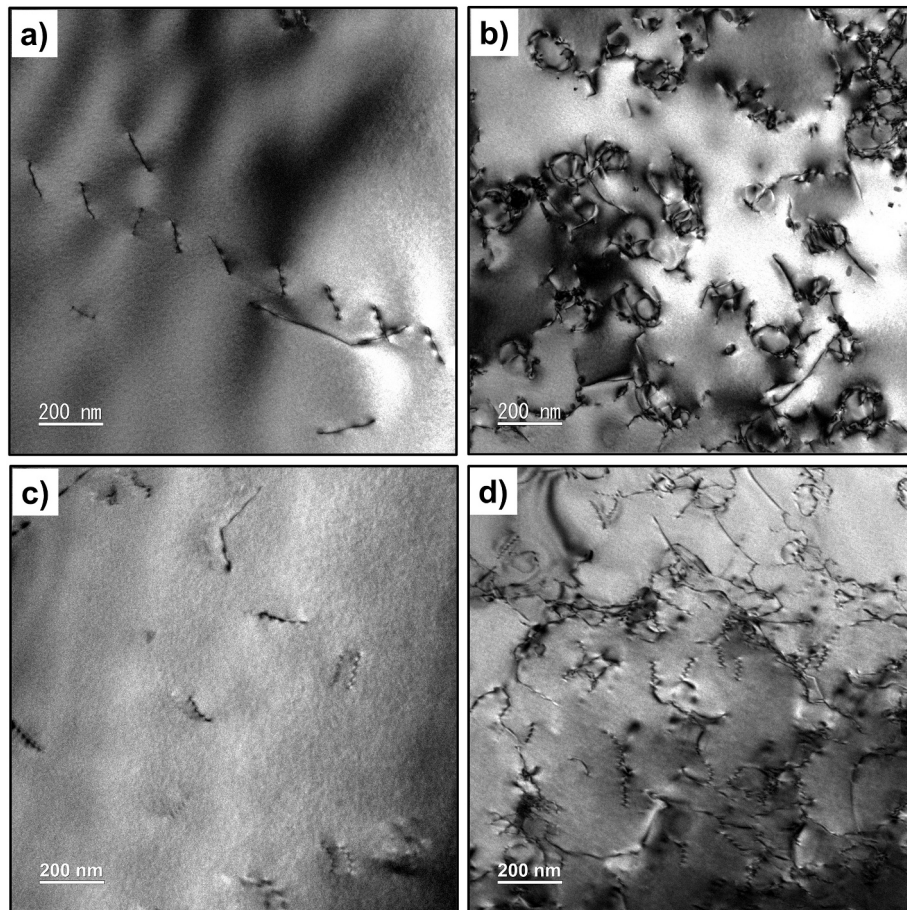

Fig. 3. Dislocations in a) BM (as-rec.); acquired in [001] zone axis and b) gauge part of sample after 34,220 h at 700 °C/165 MPa; acquired in [001] zone axis; c) BM (as-rec.); acquired in two-beam condition and d) gauge part of sample after 34,220 h at 700 °C/165 MPa; acquired in two-beam condition.

Table 4

Precipitate types, locations, number densities, sizes and volume fractions in base material (BM) and 700 °C/165 MPa crept sample (gauge and head part).

Prec.	σ_{app}/ MPa	T/°C	t/ h	NS*	N_V/ m^{-3}	d	f_V/ %	Method	Loc.
MX	–	–	0	GI	See text	0.5 ± 0.2 μm	See text	TEM	BM
γ'	165	700	34,220	GI	$8.9 \cdot 10^{19}$	108 ± 45 nm	5.8	TEM	Gauge
γ'	–	700	34,220	GI	$1.3 \cdot 10^{20}$	84 ± 30 nm	3.8	TEM	Head
M$_{23}$C$_6$	165	700	34,220	GB	See text	0.4 ± 0.1 μm	See text	TEM	Gauge
M$_{23}$C$_6$	165	700	34,220	GI	$\approx 10^{20}$	50 ± 20 nm	≈ 1	TEM	Gauge
μ	165	700	34,220	GB	See text	$1-2$ μm	See text	SEM	Gauge
μ	–	700	34,220	GB	See text		See text	SEM	Head

* *Nucleation Sites (NS): GB- grain boundaries, GI- grain interior.*

Table 5

Volume phase fraction of γ' for gauge and head section after 34,220 h at 165 MPa/700 °C based on experimental evaluation (f_V), MatCalc ($f_{V,MC}$) and ThermoCalc [9] ($f_{V,TC}$).

Loc.	f_V/ %	Method	$f_{V,MC}$/ %	Source	$f_{V,TC}$/ %	Source
Gauge	5.8	Eq. (12)	5.2	MatCalc	6	ThermoCalc [9]
Head	3.8		5.2	MatCalc	6	ThermoCalc [9]

4. Model setup

Similar to the strategy proposed in [36], the input parameters have been selected according to a) literature study, b) experimental investigations from this work (such as TEM/SEM/EBSD) and c) creep test results (both from TU Graz and from the ECCC data collation for this material). An overview on all parameters for a) and b) including sources is given in Table 3.

Microstructural start values for the simulation are provided at the bottom of Table 3. The TEM measurement of the BM (as-received condition)- see Section 5.1- served as a start input for the mobile dislocation density $\rho_{m,0}$. The observed $\rho_{m,0} = 4 \cdot 10^{13}\, m^{-2}$ is supported by literature data on A617 base material [4,9] in a similar range. The grain size (respectively the grain radius R_{gb}) in our material was determined by EBSD and is kept at a constant level during the creep simulation.

5. Results and discussion

5.1. Dislocation- and grain structures

EBSD evaluation of the 700 °C sample after 34,220 h of creep at 165 MPa yields a grain size of approximately 400 μm in the head section (see Fig. 2a-b) and of 500 μm in the gauge section (see Fig. 2c-d). In the BM in as-received condition (see Fig. 1), the grain size is in a very similar range. Around 2/3 of all detected interfaces are twin boundaries, with a predominating coincidence site lattice (CSL) of $\sum 3$. The rest of all interfaces (around 1/3) represent high-angle grain boundaries (HAGBs) with a misorientation angle larger than 15°. The shown HAGBs (see Figs. 1b, 2b, d) are subdivided into two to three blocks by the twins. Before the start of creep (in as-received state), most dislocations according to the geometrically necessary dislocation (GND) map in Fig. 1a are located along HAGBs. The density of GNDs in the base material (BM) amounts to an average of $3.5 \cdot 10^{12}\, m^{-2}$, with a distribution "BM" for the individually analyzed pixels as given in Fig. 2e.

After 34,220 h of creep at 700 °C and 165 MPa, the dislocations positioned along the grains have been annihilated in the head section by static recovery (see Fig. 2a). This is in line with a slight decrease of the GND density to approximately $2.1 \cdot 10^{12}\, m^{-2}$ in the head section of the crept sample, as can be seen in Fig. 2e by the label "700 °C(h)". By contrast, the gauge section of the crept sample is characterized by a strong release of dislocations from the grains (as indicated in the GND map of Fig. 2c). An increase of the GND density to around $6.2 \cdot 10^{12}\, m^{-2}$ can be seen in Fig. 2e, labelled as "700 °C(g)". In the gauge part of the crept sample, there seems to be a local concentration of plastic
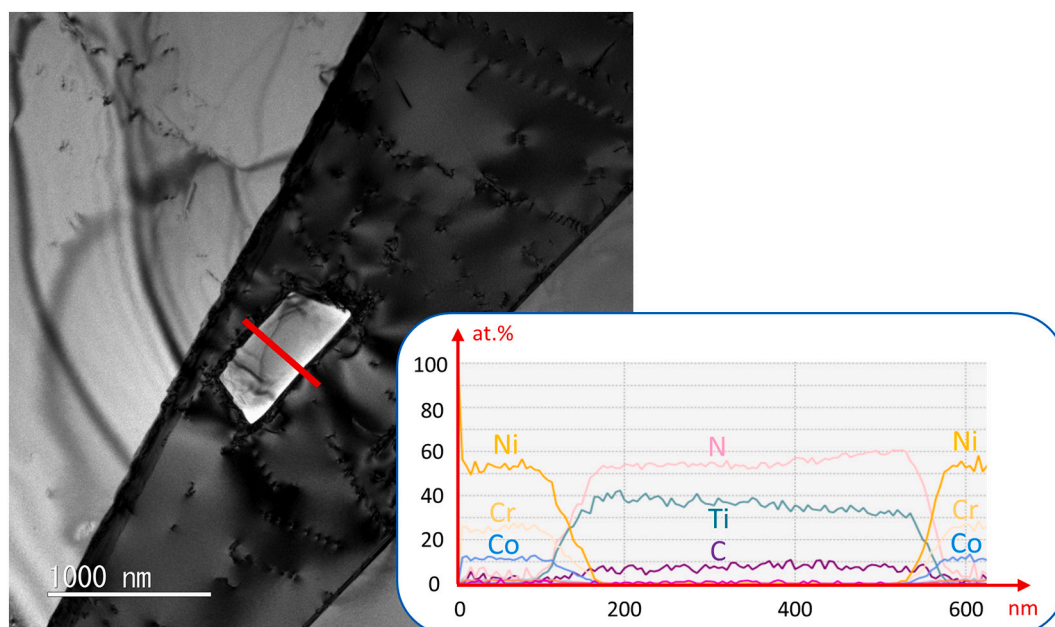
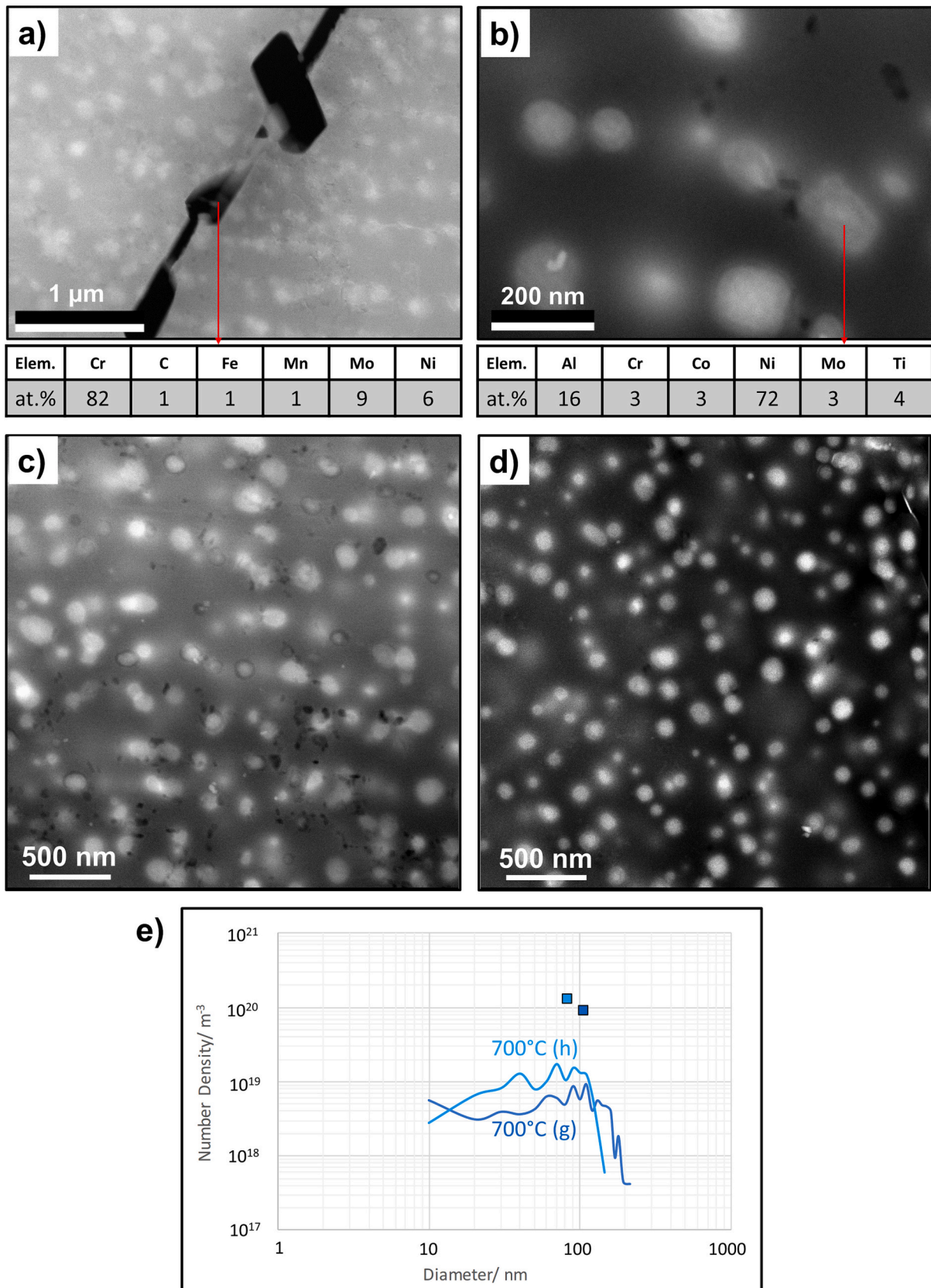**Fig. 4.** TEM-EDX line scan of Ti-rich MX found in the BM (as-received condition).

a)

Elem.	Cr	C	Fe	Mn	Mo	Ni
at.%	82	1	1	1	9	6

b)

Elem.	Al	Cr	Co	Ni	Mo	Ti
at.%	16	3	3	72	3	4

Fig. 5. STEM micrographs with quantified EDX results of a) $M_{23}C_6$ at grain boundaries and b) of γ' after 34,220 h of creep at 700 °C/165 MPa; c-d) overview of γ' precipitates after 34,220 h at 700 °C/165 MPa in c) gauge and d) head section; e) evaluated size distribution of γ' in gauge (g) and head (h) after 34,220 h at 700 °C/165 MPa.
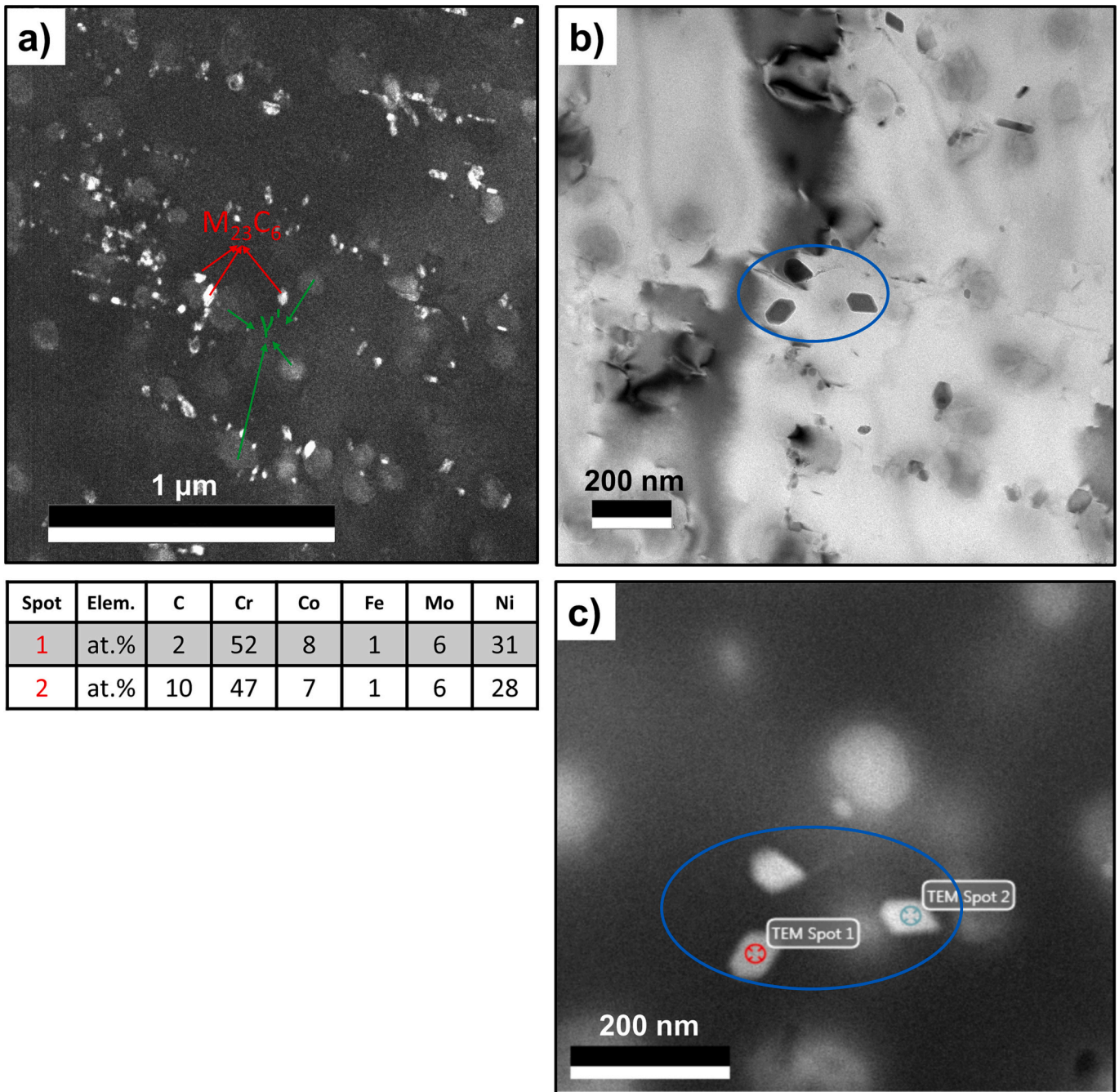
Fig. 6. a) $M_{23}C_6$ and γ' in grain interior in 700 °C/165 MPa crept condition of gauge (TEM dark field); b) TEM-bright-field of $M_{23}C_6$ carbides in the grain interior after creep at 700 °C/165 MPa (gauge); c) identification of $M_{23}C_6$ by EDX in TEM dark-field (see table left for spots 1 and 2).

Spot	Elem.	C	Cr	Co	Fe	Mo	Ni
1	at.%	2	52	8	1	6	31
2	at.%	10	47	7	1	6	28

deformation that leads to the formation and alignment of slip bands (visible as green areas in Fig. 2c). This localization of deformation predominantly occurs along HAGBs and is less visible along twin boundaries. This indicates that twins do not promote a strong pile-up of dislocations. Recrystallization does not occur, but in the gauge section, some mobility of a low number of twin boundaries can be observed in Fig. 2d, since these appear serrated.

Dislocation densities were first estimated from TEM investigations of the BM (see Fig. 3a) and the gauge part of the crept sample after 34,220 h at 700 °C/165 MPa (see Fig. 3b) in the zone axis [001]. Therefore, a mean linear intercept method from [34] was applied. The result of the dislocation density in the BM (in as-received condition) was $4 \cdot 10^{13}$ m^{-2}, incorporating a sample thickness of 100 nm detected by EELS [35]. In contrast, an increase of one order of magnitude up to $2 \cdot 10^{14}$ m^{-2} was

found in the gauge part of the crept sample, when using a measured sample thickness of 130 nm according to the EELS log-ratio technique [35].

In addition, dislocation densities in BM and the gauge part of the crept sample after 34,220 h at 700 °C/165 MPa were evaluated in two-beam condition. Analysis yielded a dislocation density of $3 \cdot 10^{13}$ m^{-2} for the BM (see Fig. 3c) and of $2 \cdot 10^{14}$ m^{-2} for the crept sample after 34,220 h (see Fig. 3d). This result is close respectively identical to the one in the [001] zone axis.

These two values are important for the creep simulation. Whereas the dislocation density from the as-received BM serves as an input parameter, the crept condition helps to verify the microstructural correctness of our A617 creep model that will be shown in the following.
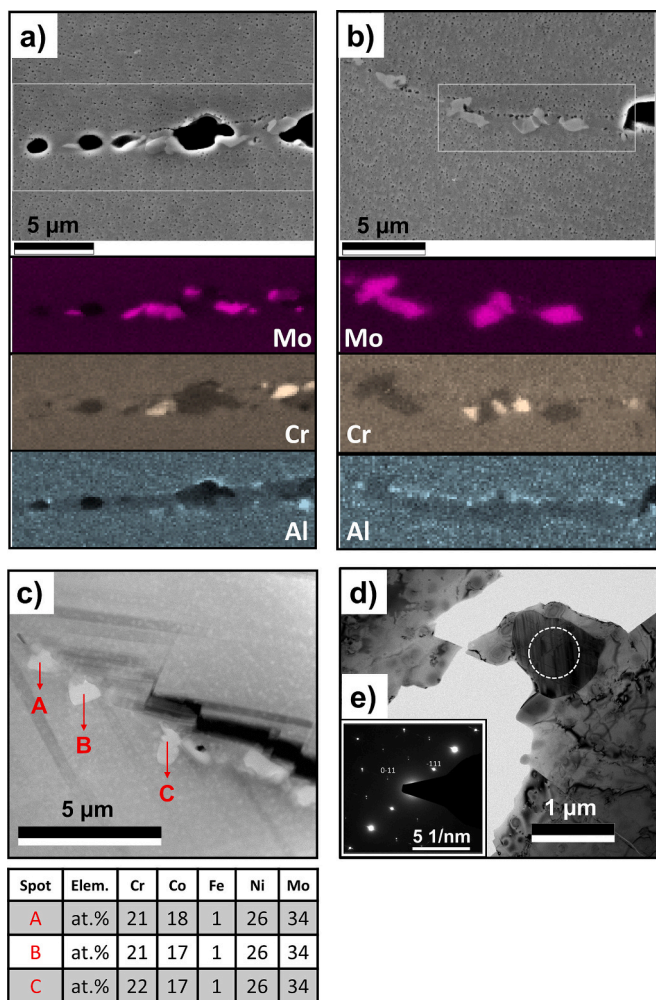
Fig. 7. a-b) Mo, Cr, Al maps from SEM for precipitates at HAGBs in 700 °C/165 MPa crept condition (gauge); c) μ-phase found along HAGBs (close to cracks) identified by TEM-EDX after creep at 700 °C/165 MPa; d) μ-phase with stacking faults characterized by e) TEM-SAD.

Table 6

Chemical composition of μ-phase in at.% according to TEM-EDX, MatCalc and literature.

Unit	Co	Cr	Fe	Mo	Ni	Source
At.%	17–18	21–22	1	34	26	TEM-EDX
	22.5	17.2	3.1	31.8	25.4	MatCalc
	22	23	–	32	23	[59]

Table 7

Equilibrium phase fractions of A617 from MatCalc.

Precipitate	650 °C	700 °C	750 °C
	[%]	[%]	[%]
γ'	6.54	5.19	3.71
$M_{23}C_6$	1.34	1.31	1.12
M_6C	–	–	0.22
μ-Phase	6.56	3.82	1.15
MX	0.15	0.16	0.17

5.2. Precipitate state

The following Table 4 provides an overview of all detected precipitates in TEM and SEM. Where possible, size (diameter d), number density (N_V) and phase fraction (f_V) were accurately determined. In case
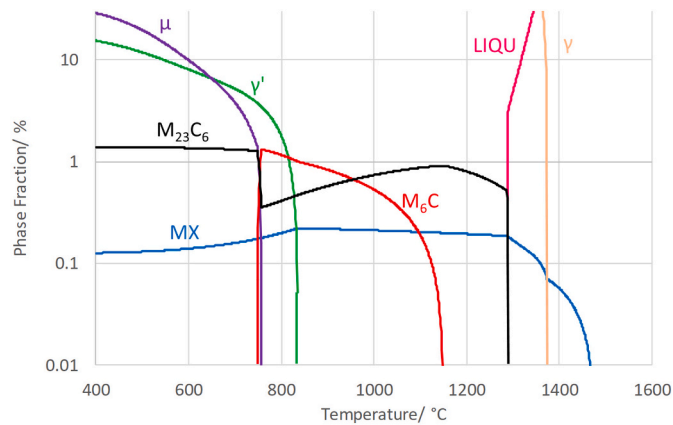

Fig. 8. Equilibrium phase fractions for alloy 617 between 400 and 1600 °C.

of rare or insufficient number of characterized particles, only the size was stated. f_V of γ' was calculated from eq. (12), whereas N_V was evaluated by eq. (13) from [56]. t_S is the sample thickness (100 nm for the gauge- and 80 nm for the head sample), N_A is the area density, and A_{sample} denotes the investigated sample area. Table 5 compares f_V values of γ' from eq. (12) with thermodynamic calculations.

$$f_V = \frac{d^3 \pi}{6} \bullet N_V \tag{12}$$

$$N_V = \frac{1}{A_{sample}} \bullet \sum_{i=1}^{N_A} \frac{1}{t_S + d_i} \tag{13}$$

TEM investigations only revealed a rare number of Ti-rich MX carbonitrides with a size of approximately 0.5 μm in the BM (see Fig. 4 including an EDX line scan). No γ' nor any $M_{23}C_6$ precipitates were found in the BM (as-received condition).

After 34,220 h of creep at 700 °C and 165 MPa, γ' and $M_{23}C_6$ were characterized both by TEM-EDX (as can be seen in Figs. 5a-b) and by SAD.

The mean size (diameter) d of γ' turned out to be 108 nm in the gauge part and 84 nm in the head section of the sample. The number density N_V of γ' according to eq. (13) from [56] yielded $8.9 \cdot 10^{19}$ m^{-3} in the gauge- and $1.3 \cdot 10^{20}$ m^{-3} in the head section of the sample. An impression of the number density in gauge and head is provided in Figs. 5c-d. The evaluated size distribution of γ' for gauge and head section based on eq. (13) is shown in Fig. 5e.

According to eq. (12), the phase fractions (f_V) of γ' amount to 5.8% for the gauge section, respectively to 3.8% for the head section of the crept sample, see Table 5. Both of them fit well to the thermodynamic equilibrium result from MatCalc which suggests a phase fraction of 5.2% (please refer to Section 5.3). Volume fraction data on γ' from literature are scarce. Krishna et al. [9] report a comparable equilibrium phase fraction of approximately 6% calculated by ThermoCalc. This high level of the γ' phase fraction was experimentally verified for the as-received condition (BM) in [9], but was observed to drop during service due to excessive nucleation of TiN [9]. This differs from our alloy in two aspects: i.) In our case, γ' was not found in the as-received condition (BM), because in contrast to [9], we did not temper our material after solutionizing. ii.) In our A617, only a low N-content is present, which makes TiN formation rare and leaves the γ' phase fraction almost unaffected.

The mean diameter of chromium-carbides $M_{23}C_6$ located at grain boundaries (GBs) was around 0.4 μm (see Table 4 and Fig. 5a). A second and much finer population of $M_{23}C_6$ was found in the grain interior with a size of approximately 50 nm (see Fig. 6a-c).

The quantity of $M_{23}C_6$ in the grain interior can be roughly estimated by applying eq. (14)- adopted from [56]- to Fig. 6a which portrays the
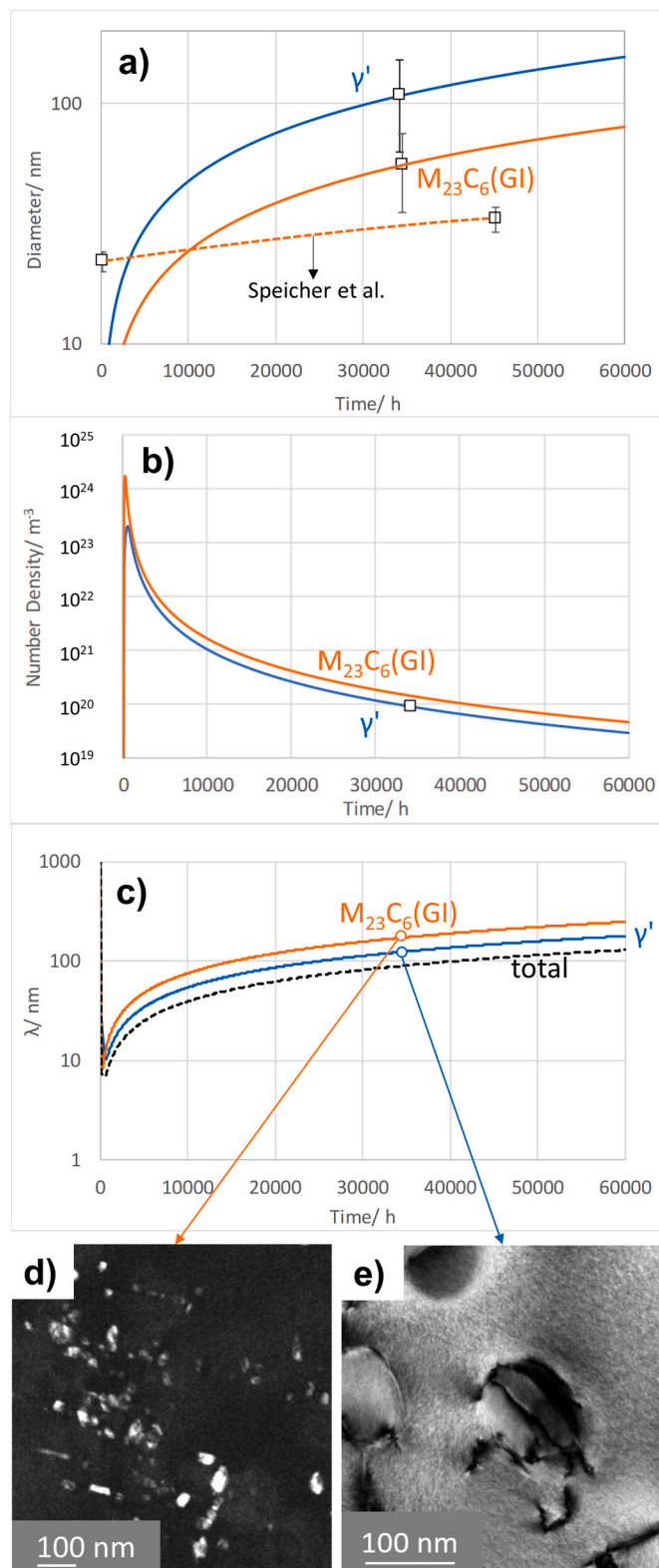
Fig. 9. a) Diameter evolution of $M_{23}C_6$ (GI-grain interior) and γ' during creep at 700 °C (fitted to TEM data from this work); the dashed line are $M_{23}C_6$ (GI) data from Speicher et al. [4]; b) number density evolution of $M_{23}C_6$ and γ' during creep at 700 °C (calculated); c) calculated interparticle distance of $M_{23}C_6$ (GI) and γ' at 700 °C and d-e) comparison to TEM figures after 34,220 h of creep at 700 °C/165 MPa (gauge section).

crept gauge part. Since around 150 carbides can be seen within an image size of 3.59 μm², this corresponds to an area density of $N_A = 4 \cdot 10^{13}$ m^{-2}. Together with a TEM sample thickness of $t_S = 100$ nm, the number density amounts to approximately $N_V = 3 \cdot 10^{20}$ m^{-3} for the portrayed area. This number for $M_{23}C_6$ (GI) agrees well to MatCalc calculations, as will be demonstrated later (see Section 5.3).

$$N_V = \frac{N_A}{t_S + d} \tag{14}$$

SEM investigations of the crept sample confirmed the existence of coarse $M_{23}C_6$ at the GBs and in addition found a high proportion of even larger (1–2 μm) sized μ-phase occupying the boundaries. This applies for both head and gauge section of the crept sample. In the gauge part, μ-phase was particularly frequently found near or along cracks. To distinguish μ-phase from $M_{23}C_6$ and γ', element maps for Cr, Mo and Al were applied to the grain boundary zones.

Whereas μ-phase appears Mo-rich in Fig. 7a-b, Cr-rich spots are related to $M_{23}C_6$. Coarsened chains of γ' particles- which partly also concentrate along the HAGBs- can be recognized in Fig. 7a-b by an enrichment of Al in the corresponding element map. μ-phase is found along grain boundaries and close to cracks, as shown in Fig. 7a-d. μ-phase contains 20–21 at.% Cr, 17–18 at.% Co, 26 at.% Ni, 34 at.% Mo and 1 at.% Fe, respectively. This result matches with the MatCalc and literature data, as can be seen in Table 6. Inside the μ-phase, various stacking faults are visible which is also reported in literature [57,17], see Fig. 7d. The stacking faults cause satellite reflections and their streaking in diffraction patterns [58] which we indexed as a rhombohedral A_6B_7 structure, see Fig. 7e.

5.3. MatCalc equilibrium

MatCalc equilibrium identifies four phases to be stable in A617 below 750 °C: γ', $M_{23}C_6$, μ-phase and Ti-rich MX (carbo-)nitrides, as indicated, in Table 7 and in Fig. 8. Although not experimentally found in this work, M_6C formation is theoretically possible [4]. However, M_6C is metastable at 700 °C in contrast to $M_{23}C_6$ and μ-phase [18]. According to the simulation, Mo clearly prefers to enter μ-phase at 700 °C instead of forming M_6C.

For $M_{23}C_6$ carbides, MatCalc calculates an equilibrium phase fraction of 1.3% at 700 °C, which is in line with calculations in [4]. With an estimated GB surface density of $4 \cdot 10^3$ m^{-1} and around 50% of the space being occupied by either GB carbides or μ-phase (based on TEM and SEM evaluation), a phase fraction of about 0.1% can be attributed to $M_{23}C_6$ or μ-phase at GBs. Concerning the total simulated $M_{23}C_6$ phase fraction, this leaves 1.2–1.3% to finer $M_{23}C_6$ inside the grain. These numbers suggest densities in order of max. 10^{16} m^{-3} for $M_{23}C_6$ at GBs, but $>10^{20}$ m^{-3} for $M_{23}C_6$ in the grain interior (GI). These theoretical considerations are in principle confirmed by observations in Fig. 6a and also by precipitate kinetic simulations of A617B carried out by [4].

The γ' phase fraction of 5.2% (at 700 °C) from MatCalc is in good agreement with our TEM result that suggests 3.8 to 5.8% for the head and 5.5 to 8.8% for the gauge section after 34,220 h of creep at 700 °C and 165 MPa (see Tables 4, 5) and also is confirmed by data from [4].

In contrast to this, the μ-phase is strongly over-predicted by MatCalc and represents a worst-case scenario for a fully pronounced TCP formation in this material. The μ-phase is not formed by nucleation in bulk or matrix boundaries, however, but needs $M_{23}C_6$ as a precursor instead [16]. Thus, its formation appears to be very slow compared to the other precipitate types in the material, and the theoretically predicted equilibrium phase fraction will not be reached.

5.4. Precipitate evolution

For the time-dependent size evolution of measured precipitates inside the grain, the data gained from TEM were fitted to a cubic Ostwald ripening law according to [44], see Fig. 9a. To model the increase of the

Table 8
Optimized remaining input parameters for A617 creep model.

Parameter	Number	Unit	Parameter	Number	Unit
a_1	$5 \cdot 10^{-14}$	m/s	α	0.03	–
V_r	$155 \cdot \Omega = 110 \cdot b^3$	m^3	D_{vp}	$1.4 \cdot 10^{-19}$	m^2/s

precipitate phase fraction towards its equilibrium value (adopted from TEM for γ' and from MatCalc for M$_{23}$C$_6$ inside the grain), an Avrami equation was applied, as described in [60]. The evolution of number density of grain-interior M$_{23}$C$_6$(GI) and γ' was calculated from size and volume fraction (see Fig. 9b).

Finally, the interparticle distance of γ' and of M$_{23}$C$_6$ located in the grain interior (GI) was determined from eq. (5.1). As depicted by Fig. 9c, the interparticle distances (λ) of M$_{23}$C$_6$ (GI) and of γ' are close to each other with 170 nm and 120 nm after 34,220 h, respectively. The calculated λ values can be confirmed by TEM observations after 34,220 h of creep exposure at 700 °C/165 MPa, see Figs. 9d-e.

γ' and small M$_{23}$C$_6$(GI) are situated within the grain interiors and thus retard the motion of mobile dislocations. Consequently, we include these particles into the calculation of the mean obstacle spacing, see eqs. (4) and (5.2).

By contrast, the M$_{23}$C$_6$(GB) and the μ-phase along grain boundaries are considered in the frame of precipitate damage, see eqs. (11) and (11.1).

As pointed out by [32] and also illustrated in Fig. 8, the number of MX is negligible in A617. They are not thought to increase the creep strengthening (because of their large size and low number density), but also have not been observed to be involved in damage. As a result, MX precipitates are not considered for the simulation.

5.5. Simulation of creep behavior

We set up our creep simulation in order to be able to compare it against the following available experimental data:

- Experimental and reported rupture times (see Section 5.5.1, Fig. 11a)
- Reported times to 1% strain (see Section 5.5.1, Fig. 11b)
- Reported minimum creep rates (see Section 5.5.1, Fig. 12)
- Impact of ductility (see Section 5.5.2, Fig. 13)

- Microstructural evolution (see Section 5.5.3, Tables 9 and 10)

5.5.1. Predictability of time to rupture, time to 1% strain and minimum creep rate

A small number of remaining input parameters, which are not experimentally accessible, needed to be determined in an iterative process, see Table 8. Creep curves between 165 and 215 MPa were calculated in steps of 5 MPa. Reaching a cavitation damage D_{cav} of 100% served as a failure criterion so that the calculation was stopped. As an example, a simulated creep curve- i.e., a plot of strain ε over time- and the evolution of the cavitation damage parameter D_{cav} at 165 MPa/ 700 °C is shown in Fig. 10.

Variables that needed to be fixed were the pre-factor of the glide velocity, a_1, the dislocation interaction coefficient, α, the pipe diffusion coefficient, D_{vp}, and the activation volume for dislocation glide, V_r (where hints about the range were available as given in Table 3, Section 4). The reduction of area at the fracture location, Z, was chosen as 4% to reflect the worst-case scenario of brittle rupture at 700 °C according to [61]. Parameters a_1, α, D_{vp} and V_r were optimized to lie both within the experimental scatter band of ECCC from datasheet 2017 [62] in the time-to-rupture diagram (TTR) and also in order to meet our experimental rupture times.

The result of the simulated TTR diagram at 700 °C is presented in Fig. 11a, including a comparison to ECCC reference data [62] and to experimental data points from Speicher [4].

Our simulated rupture times lie well within the +20% scatter band from the ECCC [62].

In addition, our calculated data points are reasonably close to the experimentally observed results. Some deviation from parallelism compared to the ECCC reference line [62] can be observed for lower stresses (especially between 165 and 175 MPa). For a discussion on possible reasons for this behavior, please refer to Sections 5.5.4, 5.5.5 and 5.5.8.

Fig. 11b illustrates the agreement of our creep simulation between 165 and 200 MPa at 700 °C in regard to available times to 1% strain (TT1%) from literature. Our simulation result lies in the upper half of a 30% scatter band for TT1% which was adopted from Schubert [61]. Our simulation data also fit well to Huntington creep data [63] (which tend to be a bit weaker) and to data points from modified A617 [27] (which
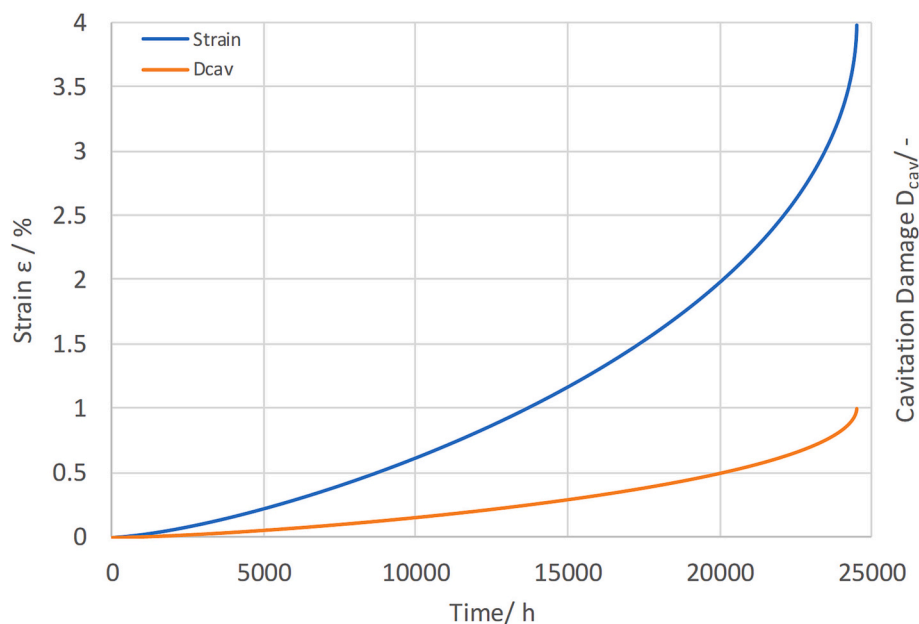

Fig. 10. Simulated creep curve (strain ε over time t) of A617 at 165 MPa/700 °C (scale on left ordinate) and evolution of cavitation damage parameter D_{cav} (scale on right ordinate).
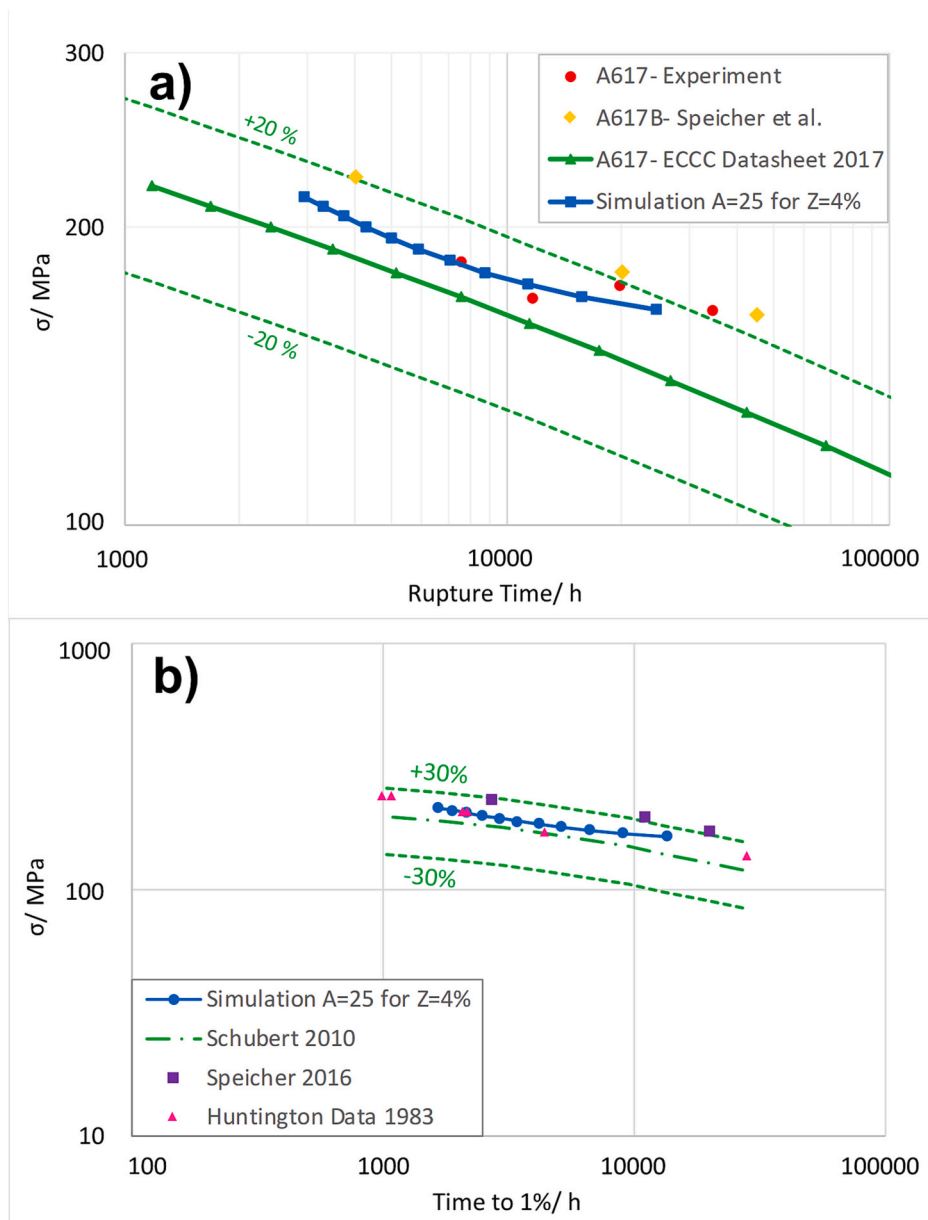
Fig. 11. a) Simulated TTR diagram at 700 °C compared to experiments (this work), ECCC datasheet 2017 [62] and data points from Speicher et al. [4]; b) Simulated times to 1% strain at 700 °C compared to data from Schubert 2010 [61], Speicher 2016 [27] and Huntington Alloys 1983 [63].

are significantly stronger due to a more advanced alloying concept). Between 175 and 200 MPa, our modelled TT1% points are perfectly parallel and extremely close to the average data provided by [61]. At lower stresses (165 to 170 MPa), there seems to be a slight trend of the simulation to deviate from the falling shape of the average TT1% data of [61] towards the upper end of the scatter band.

Evaluation of the modelled minimum creep rate (MCR) based on available literature data represents another option to validate our simulation. For this purpose, four stress conditions were analyzed: 170, 185, 200 and 215 MPa. As can be seen in Fig. 12, the calculated MCR values range from around $7 \cdot 10^{-11}$ s^{-1} at 170 MPa to about $9 \cdot 10^{-10}$ s^{-1} at 215 MPa. This is in very good agreement with MCR data from Knezevic [64], with slightly higher rates predicted by the simulation. By contrast, the MCR data from Huntington Alloys given in [63] are half to one order of magnitude higher than the simulation, showing also a pronounced scatter in the results. For comparison, two measured steady state creep rates of A617 from Oak Ridge National Laboratory [65] are shown in the diagram, underlining the large potential scatter of this material.

According to that, the MCR from the simulation are well situated within the scatter band ranges from Oak Ridge and Huntington. Our simulated MCR only show a slight downward trend at lower stresses, whereas Knezevic data [64] suggest a fully linear dependence in logarithmic scale. For a discussion on this small discrepancy, please refer to Section 5.5.5.

5.5.2. Impact of ductility on fracture time

Since the exact rupture time depends strongly on the ductility of the material [3,28], we included the reduction of area, Z, within the pre-factor of damage, A, see eq. (10). To investigate the effect on the position in the TTR diagram, Z was varied between 2 and 8% (which led to pre-factors A between 12.5 and 50). The result of the parameter study is shown in Fig. 13. The previously presented master simulation is included as a blue line (with $A = 25$ and $Z = 4$%). It turns out that for lower ductility values, rupture in the simulation occurs much earlier. This tendency is confirmed by our experimental results, where early fracture took place at 170 MPa (with $Z = 4.8$%) and 185 MPa (with $Z =$
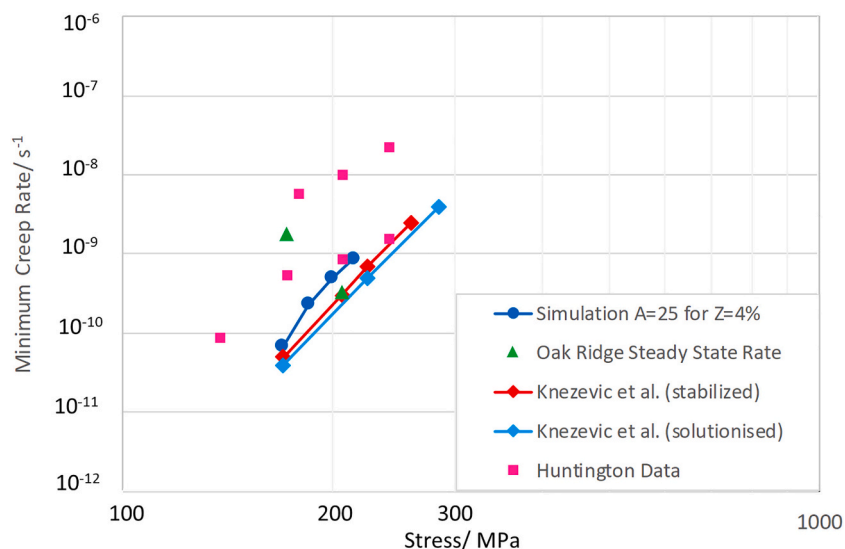
Fig. 12. Simulated MCR of A617 for 170, 185, 200 and 215 MPa at 700 °C compared to steady state rates from Oak Ridge 1985 [65], MCR from Knezevic 2013 [64] and MCR from Huntington 1983 [63].
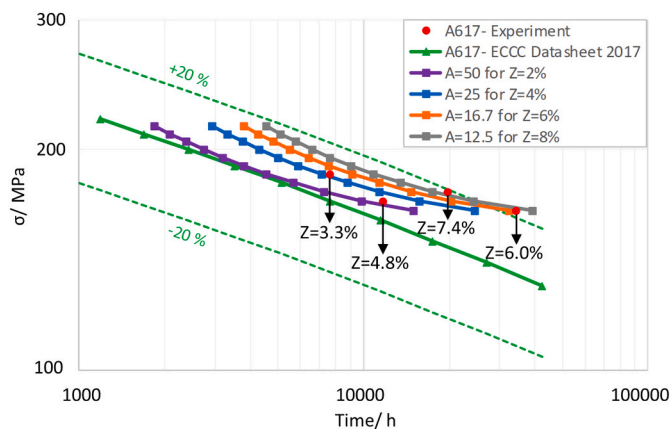

Fig. 13. Simulated TTR diagram at 700 °C with Z = 2,4,6,8% compared to experiments (this work) and reference from ECCC datasheet 2017 [62].

3.3%). The simulation anticipates a Z between 2 and 6% for the relevant data points. By contrast, for more ductile samples, lifetime in the simulation is prolonged. This is again consistent with experimental results from the samples at 165 MPa ($Z = 6.0\%$) and 175 MPa ($Z = 7.4\%$). Simulation results in a reduction of area between 6 and 8% for the corresponding rupture times. Surprisingly, for the portrayed stress range of between 165 and 215 MPa at 700 °C, approximately the entire +20% scatter band is filled, when varying the ductility from $Z = 2$ to 8%.

Both simulation and measurements point out the importance of ductility for modelled and real creep life. We succeeded in finding a correlation between the reduction of area, the degree of damage in the material and reachable rupture times. A number of reasons might be responsible for the low level of ductility in our samples: i.) The material history of our samples- specifically, the missing annealing heat treatment at 980 °C [25]. ii.) Formation of brittle μ-phase [17] which we found in our material at grain boundaries. Iii.) The low selected stresses in experiment (165 to 185 MPa in our case), since stresses ≤200 MPa at 700 °C can lead to decreased ductility in some heats [10,26–28]. iv.) Segregation phenomena involving S and B [28].

In terms of creep modelling, it might be meaningful to distinguish ductile from brittle failure behavior. Whereas ductile rupture can be sufficiently described by reaching a critical strain value, a critical proportion of cavitation at grain boundaries might have to be defined for brittle rupture, as pointed out in [66,67]. As a future task, coupling our creep model with a physical cavitation evolution law is recommendable in order to improve predictivity.

5.5.3. Microstructural verification

Every calculated point in the TTR diagram illustrated previously is accompanied by a simulated microstructural evolution. In fact, creep deformation in our model is the consequence of mobile dislocations moving via a certain stress- and temperature-dependent effective velocity, as stated by Orowan's law in eq. (1). The following Table 9 indicates the modelled microstructural changes between the BM (as-received condition) and the crept stage at 700 °C (with stresses from 165 to 200 MPa and $Z = 4\%$). Results for stresses from 205 to 215 MPa are in line with the trend of 165–200 MPa.

Mobile dislocation densities ρ_m increase at all investigated stresses, compared to the BM (in as-received condition): the increase is by a factor of 2 at 165 MPa, 10 at 180 MPa and 30 at 200 MPa, at time of rupture, respectively. The simulated evolution of ρ_m is presented in Fig. 14 for 165, 175 and 200 MPa, including a comparison to TEM measurements from this work and literature values [4,68,9], see also Table 10.

It turns out that a peak of ρ_m is reached between 300 and 500 h (sooner for higher stresses, later for lower stresses) because of multi-plication/ emission of mobiles, before recovery starts to predominate and ρ_m reduces. Finally, a saturation regime comes into play towards the end of simulated creep. The jump in the evolution of ρ_m at 100 h is related to accelerated multiplication of mobiles due to a drop of the interparticle distance λ in the course of γ' and $M_{23}C_6$ nucleation, see Fig. 9c.

Static dislocation density ρ_s halves to around $2.2 \cdot 10^{12}$ m^{-2} at 165 MPa and remains approximately constant at 170 MPa. Above 175 MPa, slight increases of ρ_s occur. However, the total share of static dislocations seems to be negligible compared to the significant increase in mobiles.

A comparison of climb (v_c) and glide velocities (v_g) allows further interesting insights into the creep behavior of A617. It turns out that v_c always exceeds v_g, with the result that climb governs creep of A617 in the investigated stress range. The ratio of v_c:v_g moves between 2.1 and 3.7 between 165 and 200 MPa at 700 °C. The reason for the increase in the v_c:v_g ratio with higher stresses lies in the slightly rising climb velocity, whereas the glide velocity shows a considerable reduction with stress. This drop of v_g can be traced back to stronger internal stresses due

Table 9
Overview on microstructural results from the A617 creep model at 700 °C and 165 to 200 MPa.

	Unit	Start	σ_{app}/ MPa							
			165	170	175	180	185	190	195	200
$t_{R,mod}$	h	–	24,496	15,648	11,339	8776	7074	5868	4974	4285
ρ_m	m^{-2}	$4.0 \cdot 10^{13}$	$7.8 \cdot 10^{13}$	$1.7 \cdot 10^{14}$	$2.8 \cdot 10^{14}$	$4.2 \cdot 10^{14}$	$5.8 \cdot 10^{14}$	$7.7 \cdot 10^{14}$	$9.9 \cdot 10^{14}$	$1.2 \cdot 10^{15}$
ρ_s	m^{-2}	$4.0 \cdot 10^{12}$	$2.2 \cdot 10^{12}$	$4.0 \cdot 10^{12}$	$6.1 \cdot 10^{12}$	$8.4 \cdot 10^{12}$	$1.1 \cdot 10^{13}$	$1.4 \cdot 10^{13}$	$1.6 \cdot 10^{13}$	$1.9 \cdot 10^{13}$
v_g	m/s	–	$8.5 \cdot 10^{-15}$	$7.5 \cdot 10^{-15}$	$6.9 \cdot 10^{-15}$	$6.6 \cdot 10^{-15}$	$6.3 \cdot 10^{-15}$	$6.0 \cdot 10^{-15}$	$5.8 \cdot 10^{-15}$	$5.7 \cdot 10^{-15}$
v_c	m/s	–	$1.8 \cdot 10^{-14}$	$1.9 \cdot 10^{-14}$	$1.9 \cdot 10^{-14}$	$2.0 \cdot 10^{-14}$	$2.0 \cdot 10^{-14}$	$2.1 \cdot 10^{-14}$	$2.1 \cdot 10^{-14}$	$2.2 \cdot 10^{-14}$
v_{eff}	m/s	–	$8.4 \cdot 10^{-15}$	$7.4 \cdot 10^{-15}$	$6.9 \cdot 10^{-15}$	$6.5 \cdot 10^{-15}$	$6.2 \cdot 10^{-15}$	$6.0 \cdot 10^{-15}$	$5.8 \cdot 10^{-15}$	$5.7 \cdot 10^{-15}$
λ_{all}	Nm	–	71	53	43	36	31	28	25	22
h_b	Nm	12	40	28	22	19	16	14	12	11

to higher dislocation densities.

Another analysis of the A617 creep behavior is possible by reading out the mean obstacle spacing from eq. (4), h_b, which consists of the dislocation densities, ρ_m and ρ_s, as well as the interparticle spacing λ. At 165 MPa, the distances between obstacles are around 40 nm. This value drops strongly to around 11 nm for 200 MPa. The reason for is the higher dislocation density ρ_m at 200 MPa, and the smaller λ due to the finer precipitates stemming from a shorter time for particle coarsening.

Our simulation implies the general trend of increasing dislocation density ρ_m at time of fracture with increasing applied stress. This finding is supported by the available dislocation density measurements from the literature at 164 and 175 MPa as well as by our own experimental results at 165 MPa, see Table 10. The literature data at 200 MPa are lower compared to our modelling result. This deviation is most likely caused by a relatively low correction factor of 1.2 for non-visible dislocations in the TEM micrographs as suggested by the authors [9], as opposed to a factor of 2 as stated by e.g. [34].

5.5.4. Debate on selected input parameters

Most input parameters can be taken directly from literature or from microstructural start values based on our TEM and EBSD results (see Table 3). However, a small number of parameters have to be set partially based on our experimental results (see Table 8).

5.5.4.1. Activation volume V_r.
In a previous work, V_r was deduced from stress relaxation tests, see [36]. These tests are not available in the case of A617 at 700 °C. Subsequently, the range of V_r had to be estimated based on literature on pure Ni. Wang et al. [54] suggest a range of $100–250 \cdot b^3$, with a tendency to higher values for large grain sizes and

Table 10
Modelled, measured (A: in the [001] zone axis; B: in two-beam condition) and literature data on dislocation densities in grain interiors at time of fracture.

Stress	Base material	164 MPa	165 MPa	175 MPa	200 MPa
Modelled (this work)	$4.0 \cdot 10^{13}$ m^{-2}	–	$7.8 \cdot 10^{13}$ m^{-2}	$2.8 \cdot 10^{14}$ m^{-2}	$1.2 \cdot 10^{15}$ m^{-2}
Experiment A (this work)	$4 \cdot 10^{13}$ m^{-2}	–	$2 \cdot 10^{14}$ m^{-2}	–	–
Experiment B (this work)	$3 \cdot 10^{13}$ m^{-2}	–	$2 \cdot 10^{14}$ m^{-2}	–	–
Experiment (literature)	$2.6 \cdot 10^{13}$ m^{-2}	$1.4 \cdot 10^{14}$ m^{-2}	–	$9 \cdot 10^{14}$ m^{-2}	$3.5 \cdot 10^{14}$ m^{-2}
Source	[4]	[4]	–	[68]	[9]

high stresses. Manonukul et al. [30] support the higher end of this estimate with $245–263 \cdot b^3$ at a very high stress level of 400 MPa for C263. A collection of V_r data on pure Ni from various literature sources is offered by [55], suggesting an extrapolated $V_r = 125 \cdot b^3$ for our grain size of 500 μm. As already pointed out in [36], the experimentally determined V_r can scatter by at least 10–20%. Within this range, a V_r of $110 \cdot b^3$ provided the best agreement to our measured fracture times.

5.5.4.2. Dislocation interaction coefficient.
α impacts the steepness of the simulated data points in the TTR diagram. α was therefore optimized to achieve a high degree of parallelism with the ECCC reference data line [62] and our experimental results. It turned out that $\alpha = 0.03$ led to the best agreement, although for low stresses, a slight tendency to longer
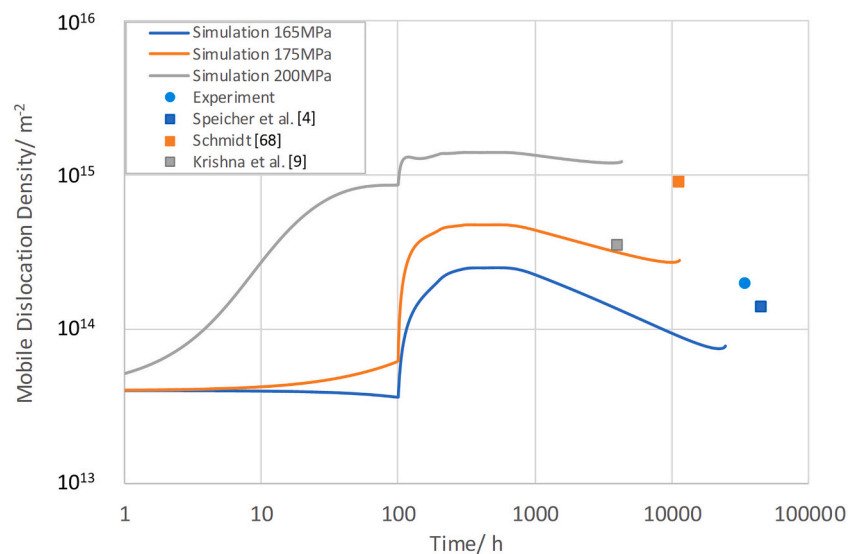

Fig. 14. Evolution of mobile dislocation density ρ_m during simulated creep of A617 at 165 MPa, 175 MPa and 200 MPa/700 °C, including a comparison to measurements (this work) and literature [4,68,9].
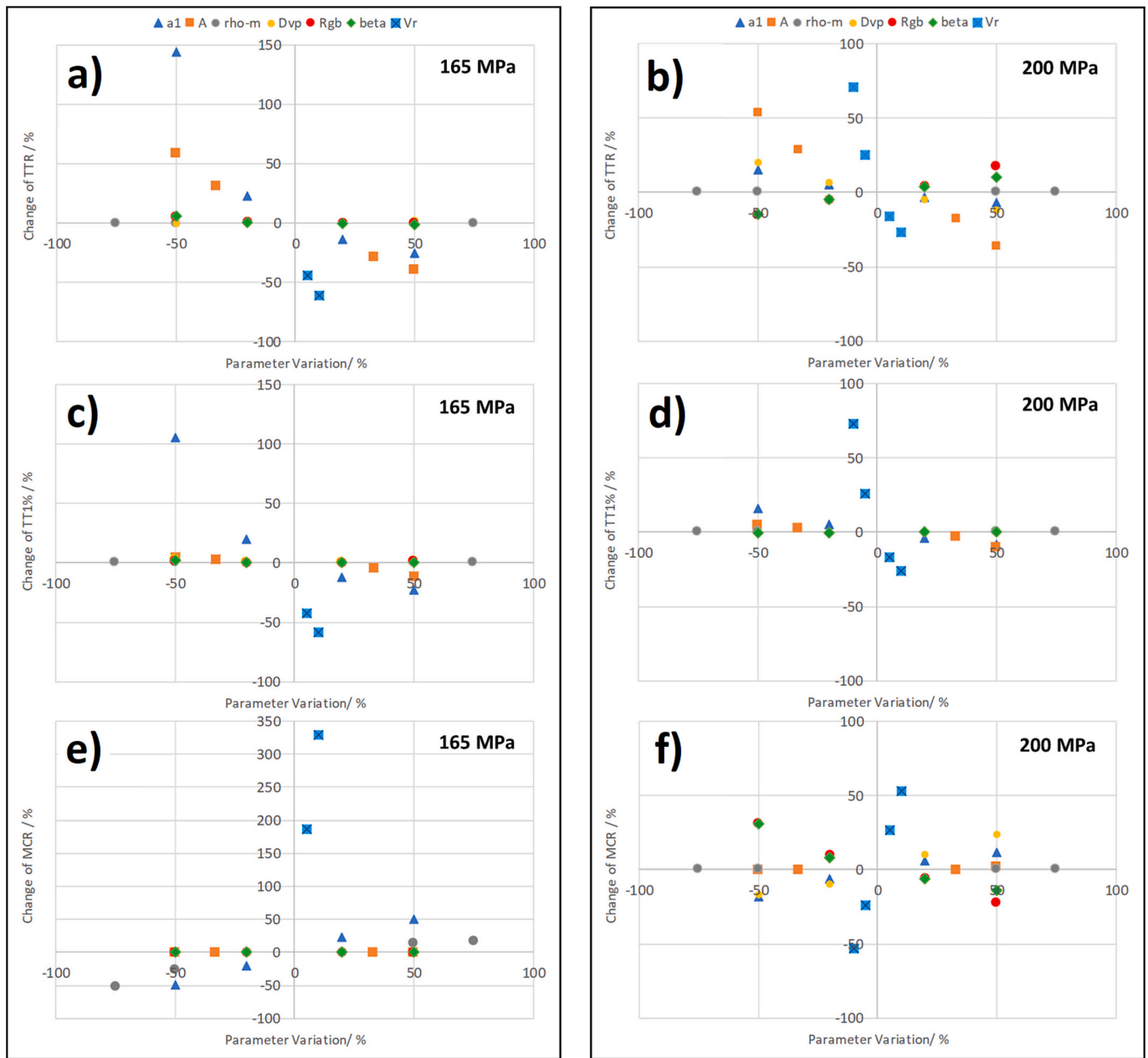
Fig. 15. Sensitivity analysis, investigating effects of a_1, A, ρ_m, D_{vp}, R_{gb}, β & V_r changes on: a) TTR at 165 MPa, b) TTR at 200 MPa, c) TT1% at 165 MPa, d) TT1% at 200 MPa, e) MCR at 165 MPa, f) MCR at 200 MPa.
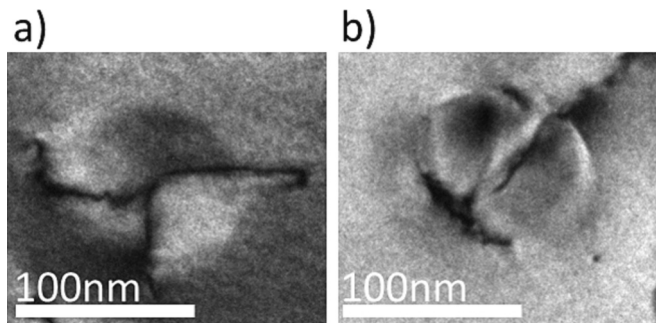

Fig. 16. γ' precipitate passed a) by climb of a dislocation split into partials and b) by cutting.

creep times can be recognized. The reason might be the growing importance of diffusion creep. According to [42], α in most metallic materials lies between 0.1 and 0.4. [69], e.g. state an α value of 0.3 for fcc metals. The discrepancy to our α = 0.03 can be explained in part by the Basinski correction for the internal stress in the case of heterogeneous dislocation arrangements [42], which is $ln\left[1/\left(b \bullet \sqrt{\rho}\right)\right]$. In our case, the Basinski correction lies within the range of factor 5–7, suggesting an effective value of α = 0.05. Moreover, α during creep has been shown to decrease with rising creep strains respectively for longer creep times [42].

5.5.4.3. Pre-factor of the glide velocity. a_1 is per se not accessible to direct measurement. However, a reasonable choice of a_1 is required to achieve realistic glide velocities of $5 \cdot 10^{-15}$ to 10^{-14} m/s. An indirect verification of the glide velocity is possible by inserting reported minimum creep rates (10^{-9} to 10^{-10} s^{-1}) and dislocation densities ρ_m
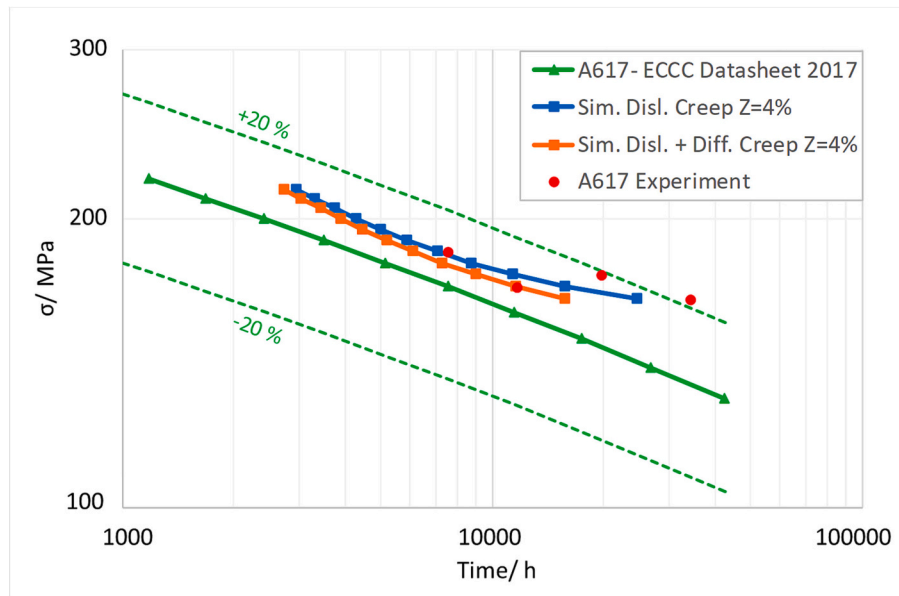
Fig. 17. Simulated TTR diagram at 700 °C for Z = 4% showing the influence of overlaid diffusion creep.

between 10^{14} and 10^{15} m^{-2} to Orowan's law, see eq. (1). When neglecting the damage factors, one arrives again at approximately 10^{-14} m/s. Factor a_1 is related to the interaction of dislocations with solutes during glide. Determination of density and distribution of solutes is beyond the scope of this work. However, a reduced availability of solute strengtheners (such as Mo or Co, which are consumed by μ-phase) after long creep exposure, might potentially increase a_1. This represents one of the possible reasons for the deviation of simulated TTR from ECCC reference data [62] at 165-170 MPa/700 °C, see Fig. 10a.

5.5.5. Sensitivity analysis and parameter study of input parameters

To estimate the impact of parameter changes on calculated time to rupture (TTR), time to 1% strain (TT1%) as well as on minimum creep rate (MCR), a sensitivity analysis was carried out for the model at 165 MPa and at 200 MPa/700 °C. The result of this study is shown in Fig. 15.

At low applied stress (165 MPa), a_1 (the pre-factor of the glide velocity), A (the cavitation damage pre-factor related to ductility) and V_r (activation volume) have the biggest impact on TTR and TT1%, see Fig. 15a and c. At high applied stress (200 MPa), the grain size R_{gb}, the density of dislocation sources β and the pipe diffusion coefficient D_{vp} additionally become important input parameters for TTR and TT1%, see Fig. 15b and d.

The strongest change of MCR at 165 MPa is caused by variations of V_r, a_1 and ρ_m, see Fig. 15e. Subsequently, a too low selected level of ρ_m might be responsible for the downward deviation of the simulated MCR at 165 MPa in contrast to the Knezevic data [64] with linear dependence, see Fig. 12. At 200 MPa, V_r, R_{gb}, β and D_{vp} determine the simulated MCR, whereas changes of ρ_m at this high stress level only have a minor effect on MCR, see Fig. 15f.

5.5.6. Experimental observations on creep damage

Our observations in EBSD (based on the GND maps) suggest a concentration of deformation and damage propagation along grain boundaries. Elemental maps in SEM and STEM-EDX spectra proved the existence of coarse μ-phase alternating with $M_{23}C_6$ along grain boundaries. μ-phase was often located close to creep cavities and cracks. Both facts support our model, where we decided to include μ-phase and $M_{23}C_6$(GB) into the precipitate damage concept.

Near grain boundaries, γ' precipitates appear to coarsen faster during creep exposure, compared to the grain interior. One reason is presumably the higher effective diffusion coefficients close to the grain

boundaries. In addition, μ-phase formation at the grain boundaries leads to a local depletion of Mo, whereas literature indicates, that high Mo-levels in the matrix effectively hinder γ' coarsening [13,45]. In general, the consumption of solid solution elements (such as Mo and Co) by the μ-phase is supposed to locally soften and weaken the material [18].

5.5.7. Interaction of dislocations with γ'

Fig. 3b suggests that the majority of γ' precipitates promote the formation of Orowan loops, when being passed by mobile dislocations. Some γ' precipitates are surmounted by climb, as illustrated in Fig. 9e. The dislocations themselves are sometimes split into partials, such as during the climb process portrayed in Fig. 16a. In very rare cases, a cutting process may occur (see Fig. 16b), but it does not seem to be a predominant mechanism at the investigated creep conditions of 165 MPa/ 700 °C.

5.5.8. Influence of diffusion creep for low stresses

For stresses ≤175 MPa, we observed a deviation of parallelism between our simulated points and the ECCC data in the TTR diagram. To investigate the impact of additional diffusion creep, we add a coble creep share [70] as stated in eq. (15) to our dislocation creep rate from eq. (1).

$$\dot{\varepsilon}_{coble} = A_c \frac{D_{gb}\delta_{gb}\sigma_{app}\Omega}{\left(2R_{gb}\right)^3 k_B T} \tag{15}$$

We implement a pre-factor of $A_c = 48$ [70,71], a grain boundary diffusion coefficient of $D_{gb} = 3.4 \cdot 10^{-12}$ m^{-2} [72] and a grain boundary width of $\delta_{gb}=5b$ [73]. As illustrated in Fig. 17, a much higher degree of parallelism between simulation and the ECCC reference line can be achieved in this way especially for 165 and 170 MPa. Diffusion creep indeed appears to play an important role in the investigated stress range, and the share of diffusion creep rate below 180 MPa potentially reaches the same order of magnitude of 10^{-10} s^{-1} as the dislocation creep rate. The accuracy of the simulation for low stresses increases, if taking diffusion creep into account.

6. Conclusion

A dislocation creep model for alloy 617 based on strengthening from grain interior $M_{23}C_6$ and γ' was developed and successfully applied in a stress range from 165 to 215 MPa at 700 °C. The creep model considers

the time-evolution and/or interaction of mobile dislocations, static dislocations, grain boundaries and precipitates and its impact on the creep rate and fracture time. Creep voids formed at grain boundaries close to large μ-phase precipitates and $M_{23}C_6$ particles. Subsequently, precipitates at grain boundaries as well as material ductility were included into damage models, specifically indicating the time of fracture.

Our creep modelling results were verified based on times to 1% strain, minimum creep rates and rupture data. We achieve good agreement with the available experimental creep and microstructural data. In addition, our model is able to explain and illustrate the essential role of material ductility on the total lifetime.

We have also tested the impact of implementing diffusional creep in addition to our dislocation creep model. Diffusion creep appears to affect the deformation rate significantly at stresses below 180 MPa, improves the accuracy of our simulation, and complements our model.

TEM investigations on the interaction between γ' and dislocations revealed Orowan looping to play the main role during creep at 165 MPa/ 700 °C, accompanied by climb and (in very rare cases) by cutting. EBSD results reveal a high proportion of twins inside the grain boundaries, which had a size of approximately 500 μm. Deformation in the GND map of gauge part of the crept sample was concentrated along grain boundaries. GNDs in the head of the crept sample after 34,220 h showed recovery behavior, whereas in the gauge part an increase was observed. In terms of the mobile dislocation density, a rise of one order of magnitude from 10^{13} m^{-2} in the BM (as-rec.) to 10^{14} m^{-2} in the 700 °C/165 MPa crept condition after 34,220 h was seen in TEM. In this context, measurements in the zone axis were confirmed by those in two-beam condition.

These findings were well embedded within literature data and used either as input of our creep simulation or consistent with our simulation results.

CRediT authorship contribution statement

Florian Riedlsperger: Conceptualization, Methodology, Validation, Formal analysis, Data curation, Writing – original draft, Visualization. **Tomasz Wojcik:** Formal analysis, Investigation, Data curation, Writing – review & editing, Visualization. **Ricardo Buzolin:** Methodology, Formal analysis, Investigation, Data curation, Writing – review & editing, Visualization. **Gerold Zuderstorfer:** Software, Writing – review & editing. **Magdalena Speicher:** Validation, Resources, Writing – review & editing. **Christof Sommitsch:** Resources, Supervision, Project administration, Writing – review & editing. **Bernhard Sonderegger:** Conceptualization, Methodology, Writing – original draft, Writing – review & editing, Supervision, Project administration, Funding acquisition.

Declaration of Competing Interest

The authors declare that they have no known competing financial interests or personal relationships that could have appeared to influence the work reported in this paper.

Data availability

Simulation data from MatCalc and MatLab are attached to this publication as supplement (in an Excel file). Experimental raw data are available from the corresponding author upon request.

Acknowledgements

Appendix A. Appendix

The following Table 11 lists all variables used in this paper (in equations or text), providing a description and unit for them.

The following Table 12 converts all non-standard units used in this paper into SI units:

Table 11
Overview on all variables used in the paper with description and unit.

Var.	Description	Unit
a_1	Parameter for glide velocity	[m/s]
a_g	Size of unit cell	[m]
a_j	Jog height- assumed as b	[m]
A	Material specific constant for damage; $A = 1/Z$	[−]
A_c	Pre-factor for coble (diffusion) creep rate	[−]
A_{sample}	Sample area for TEM investigation	[m^2]
α	Dislocation interaction factor	[−]
b	Burgers vector for fcc	[m]
β	Parameter for density of sources	[−]
c_s	Weighting factor for statics in the internal stress	[−]
Γ	Stacking fault energy	[J/m^2]
δ_{anh}	Dislocation annihilation length	[m]
δ_{gb}	Grain boundary width	[m]
d	Precipitate size (diameter)	[m]
D_{cav}	Cavitation damage parameter	[−]
D_{gb}	Grain boundary diffusion coefficient	[m^2/s]
D_{ppt}	Precipitate damage parameter	[−]
D_s	Lattice diffusion coefficient	[m^2/s]
D_{vp}	Pipe diffusion coefficient	[m^2/s]
E_{pipe}	Activation energy for climb by pipe diffusion	[J]
f_V	Precipitate (volume) phase fraction	[−]
ε	Creep strain	[−]
$\dot{\varepsilon}$	Creep strain rate for dislocation creep	[1/s]
$\dot{\varepsilon}_{coble}$	Creep strain rate for coble (diffusion) creep	[1/s]
η_v	Transfer coefficient for defects into jogs; dependent on Γ	[−]
G	Shear modulus	[Pa]
h_b	Mean obstacle spacing	[m]
k_B	Boltzmann constant	[J/K]
k_d	Ostwald ripening parameter	[m^3/s]
k_p	Ostwald ripening parameter normalized to initial particle radius	[s^{-1}]
l_{GB}	Material specific parameter for precipitate coarsening of grain boundary precipitates ($M_{23}C_6$ and μ-phase)	[−]
L_α	Parameter for elastic interactions between dislocation/defects	[m]
L_p	Diffusion path of core-vacancy before evaporation into lattice	[m]
λ	Summed-up (total) interparticle distance of all precipitates i	[m]
λ_i	Individual interparticle distance of precipitate i	[m]
M	Taylor factor	[−]
N_A	Precipitate area density	[m^{-2}]
N_V	Precipitate (volume) number density	[m^{-3}]
$N_{V,i}$	Precipitate (volume) number density of precipitate i	[m^{-3}]
Q	Activation energy for dislocation glide	[J]
r_A	Mean projected precipitate radius	[m]
r_i	Precipitate radius of precipitate i	[m]
$r_{i,0}$	Precipitate radius of precipitate i at the start of creep	[m]
R_{gb}	Grain radius	[m]
$\rho_{m,0}$	Mobile dislocation density starting value	[m^{-2}]
ρ_m	Mobile dislocation density	[m^{-2}]
$\rho_{s,0}$	Static dislocation density starting value	[m^{-2}]
ρ_s	Static dislocation density	[m^{-2}]
σ_{app}	Applied stress	[Pa]

(continued on next page)

Table 11 (*continued*)

Var.	Description	Unit
σ_i	Internal stress	[Pa]
t	Time	[s]
t_S	TEM sample thickness	[m]
$t_{R,mod}$	Modelled rupture time	[s]
T	Temperature	[K]
U_a	Acceleration voltage	[V]
v_c	Climb velocity	[m/s]
v_{cl}	Lattice diffusion share of v_c	[m/s]
v_{cp}	Pipe diffusion share of v_c	[m/s]
v_{eff}	Effective velocity	[m/s]
v_g	Glide velocity	[m/s]
V_r	Apparent activation volume for thermally activated glide	[m³]
Ω	Atomic volume (unit cell size divided by 4 atoms in fcc)	[m³]
Z	Reduction of area in creep sample after rupture	[%]

Table 12

Conversion of non-standard units into SI units.

Measure	Non-standard units		SI units		Conversion
	Symbol	Name	Symbol	Name	
Temperature	°C	Celsius	K	Kelvin	0 °C = 273 K
Time	h	Hour	s	Second	1 h = 3600 s

Appendix B. Supplementary data

Supplementary data to this article can be found online at https://doi.org/10.1016/j.matchar.2023.112720.

References

[1] M. Akbari-Garakani, M. Mehdizadeh, Effect of long-term service exposure on microstructure and mechanical properties of alloy 617, Mater. Des. 32 (2011) 2695–2700, https://doi.org/10.1016/j.matdes.2011.01.017.

[2] W. Ren, R. Swindeman, A review on current status of alloys 617 and 230 for gen IV nuclear reactor internals and heat exchangers 1, J. Press. Vess.-T. ASME 131 (2009), 044002, https://doi.org/10.1115/1.3121522.

[3] J. Klöwer, Alloy 617 and derivatives, in: A. Di Gianfrancesco (Ed.), Materials for Ultra-Supercritical and Advanced Ultra-Supercritical Power Plants, Elsevier, 2017, pp. 547–570, https://doi.org/10.1016/B978-0-08-100552-1.00016-6.

[4] M. Speicher, F. Kauffmann, J.-H. Shim, M. Chandran, Microstructure evolution in alloy 617 B after a long-term creep and thermal aging at 700 °C, Mater. Sci. Eng. A 711 (2018) 165–174, https://doi.org/10.1016/j.msea.2017.11.004.

[5] J.A. Siefert, C. Libby, J. Shingledecker, Concentrating solar power (CSP) power cycle improvements through application of advanced materials, in: Cape Town, South Africa, 2016, https://doi.org/10.1063/1.4949177, 070030.

[6] J.K. Benz, L.J. Carroll, J.K. Wright, R.N. Wright, T.M. Lillo, Threshold stress creep behavior of alloy 617 at intermediate temperatures, Metall. Mater. Trans. A 45 (2014) 3010–3022, https://doi.org/10.1007/s11661-014-2244-y.

[7] M. Speicher, A. Klenk, K. Maile, E. Roos, Behaviour of Ni-based alloys for fossil-fired power plant components in the long-term creep regime, Adv. Mater. Res. 278 (2011) 241–246, https://doi.org/10.4028/www.scientific.net/AMR.278.241.

[8] Q. Wu, H. Song, R.W. Swindeman, J.P. Shingledecker, V.K. Vasudevan, Microstructure of long-term aged IN617 Ni-Base Superalloy, Metall. Mater. Trans A. 39 (2008) 2569–2585, https://doi.org/10.1007/s11661-008-9618-y.

[9] R. Krishna, H.V. Atkinson, S.V. Hainsworth, S.P. Gill, Gamma prime precipitation, dislocation densities, and TiN in creep-exposed Inconel 617 alloy, Metall. Mater. Trans. A 47 (2016) 178–193, https://doi.org/10.1007/s11661-015-3193-9.

[10] S. Yamasaki, M. Mitsuhara, H. Nakashima, Deformation microstructure and fracture behavior in creep-exposed alloy 617, Mater. Trans. 58 (2017) 442–449, https://doi.org/10.2320/matertrans.M2016407.

[11] S.F. Di Martino, R.G. Faulkner, S.C. Hogg, S. Vujic, O. Tassa, Characterisation of microstructure and creep properties of alloy 617 for high-temperature applications, Mater. Sci. Eng. A 619 (2014) 77–86, https://doi.org/10.1016/j.msea.2014.09.046.

[12] E. Gariboldi, M. Cabibbo, S. Spigarelli, D. Ripamonti, Investigation on precipitation phenomena of Ni–22Cr–12Co–9Mo alloy aged and crept at high temperature, Int. J. Press. Vessel. Pip. 85 (2008) 63–71, https://doi.org/10.1016/j.ijpvp.2007.06.014.

[13] H. Jiang, C. Liu, J. Dong, M. Zhang, The effect of Mo and Ti elements on long-term microstructure stability of 617B nickel-base superalloy, J. Alloys Compd. 821 (2020), 153217, https://doi.org/10.1016/j.jallcom.2019.153217.

[14] Y. Guo, Z. Zhang, R. Zhou, S. Hou, B. Wang, Microstructure and mechanical properties of alloy 617B, Trans. Nonferrous Metals Soc. China 25 (2015) 1106–1113, https://doi.org/10.1016/S1003-6326(15)63704-9.

[15] A.S. Wilson, Formation and effect of topologically close-packed phases in nickel-base superalloys, Mater. Sci. Technol. 33 (2017) 1108–1118, https://doi.org/10.1080/02670836.2016.1187335.

[16] H. Jiang, J. Dong, M. Zhang, Phase transformation of alloy 617B during 10000 h aging: an element redistribution-related process, J. Alloys Compd. 765 (2018) 586–594, https://doi.org/10.1016/j.jallcom.2018.06.229.

[17] Z. Wang, Y. Li, H. Zhao, L. Chen, Z. Zhang, D. Shen, M. Wang, Evolution of μ phase in a Ni-based alloy during long-term creep, J. Alloys Compd. 782 (2019) 1–5, https://doi.org/10.1016/j.jallcom.2018.12.081.

[18] R. Krishna, S.V. Hainsworth, S.P.A. Gill, A. Strang, H.V. Atkinson, Topologically close-packed μ phase precipitation in creep-exposed Inconel 617 alloy, Metall. Mater. Trans. A 44 (2013) 1419–1429, https://doi.org/10.1007/s11661-012-1491-z.

[19] S. Schlegel, S. Hopkins, E. Young, J. Cole, T. Lillo, M. Frary, Precipitate redistribution during creep of alloy 617, Metall. Mater. Trans. A 40 (2009) 2812–2823, https://doi.org/10.1007/s11661-009-0027-7.

[20] K. Mo, G. Lovicu, X. Chen, H.-M. Tung, J.B. Hansen, J.F. Stubbins, Mechanism of plastic deformation of a Ni-based superalloy for VHTR applications, J. Nucl. Mater. 441 (2013) 695–703, https://doi.org/10.1016/j.jnucmat.2013.03.083.

[21] J. Haan, A. Bezold, C. Broeckmann, Interaction between particle precipitation and creep behavior in the NI-base alloy 617B: microstructural observations and constitutive material model, Mater. Sci. Eng. A 640 (2015) 305–313, https://doi.org/10.1016/j.msea.2015.06.002.

[22] D. Kaoumi, K. Hrutkay, Tensile deformation behavior and microstructure evolution of Ni-based superalloy 617, J. Nucl. Mater. 454 (2014) 265–273, https://doi.org/10.1016/j.jnucmat.2014.08.003.

[23] J.M. Haan, Kriechen der teilchenverfestigten Typ-A-Legierung NiCr23Co12Mo, PhD Thesis,, RWTH Aachen, Germany, 2017, https://doi.org/10.18154/RWTH-2017-03311.

[24] D. Tytko, P.-P. Choi, J. Klöwer, A. Kostka, G. Inden, D. Raabe, Microstructural evolution of a Ni-based superalloy (617B) at 700°C studied by electron microscopy and atom probe tomography, Acta Mater. 60 (2012) 1731–1740, https://doi.org/10.1016/j.actamat.2011.11.020.

[25] J. Klöwer, R.U. Husemann, M. Bader, Development of nickel alloys based on alloy 617 for components in 700°C power plants, Procedia Eng. 55 (2013) 226–231, https://doi.org/10.1016/j.proeng.2013.03.247.

[26] A. Narayanan, K. Dubey, C.M. Davies, J.P. Dear, The creep of alloy 617 at 700 °C: material properties, measurement of strain and comparison between finite element analysis and digital image correlation, Int. J. Solids Struct. 129 (2017) 195–203, https://doi.org/10.1016/j.ijsolstr.2017.08.021.

[27] M. Speicher, D. Hueggenberg, A. Klenk, S. Zickler, K. Metzger, Materials for advanced ultra-supercritical fossil-fuel power plants: materials properties, microstructure, and component behavior, Energy Technol. 4 (2016) 187–192, https://doi.org/10.1002/ente.201500311.

[28] F. Abe, M. Tabuchi, M. Hayakawa, Influence of Data Scattering on Estimation of 100,000 hrs Creep Rupture Strength of Alloy 617 at 700 °C by Larson–Miller Method, J. Press. Vess.-T. ASME 139 (2017), 011403, https://doi.org/10.1115/1.4033290.

[29] B.F. Dyson, Microstructure based creep constitutive model for precipitation strengthened alloys: theory and application, Mater. Sci. Technol. 25 (2009) 213–220, https://doi.org/10.1179/174328408X369348.

[30] A. Manonukul, F.P.E. Dunne, D. Knowles, Physically-based model for creep in nickel-base superalloy C263 both above and below the gamma solvus, Acta Mater. 50 (2002) 2917–2931, https://doi.org/10.1016/S1359-6454(02)00119-2.

[31] M. Lapera, D. Spader, H. Ghonem, A coupled, physics-based matrix-grain boundary model for creep of carbide strengthened nickel-based superalloys - I. concepts and formulation, Mater. Sci. Eng. A 769 (2020), 138421, https://doi.org/10.1016/j.msea.2019.138421.

[32] D. Spader, M. Lapera, H. Ghonem, A coupled, physics-based matrix-grain boundary model for creep of carbide strengthened nickel-based superalloys - II. Experimental results and model application, Mater. Sci. Eng. A 769 (2020), 138355, https://doi.org/10.1016/j.msea.2019.138355.

[33] A. Riva, M. Spindler, R. Krein, O. Tassa, E. Poggio, The new ECCC Datasheet for Alloy 617: multi-regime models to cover a wide range of temperature, in: Proc. 5th Int. ECCC Creep & Fracture Conf., Oct. 2021, pp. 267–280. Online Event.

[34] C.G. Panait, A. Zielińska-Lipiec, T. Koziel, A. Czyrska-Filemonowicz, A.-F. Gourgues-Lorenzon, W. Bendick, Evolution of dislocation density, size of subgrains and MX-type precipitates in a P91 steel during creep and during thermal ageing at 600C for more than 100,000h, Mater. Sci. Eng. A 527 (2010) 4062–4069, https://doi.org/10.1016/j.msea.2010.03.010.

[35] T. Malis, S. Cheng, R. Egerton, EELS log-ratio technique for specimen-thickness measurement in the TEM, J. Electron Micr. Tech. 8 (1988) 193–200, https://doi.org/10.1002/jemt.1060080206.

[36] F. Riedlsperger, B. Krenmayr, G. Zuderstorfer, B. Fercher, B. Niederl, J. Schmid, B. Sonderegger, Application of an advanced mean-field dislocation creep model to P91 for calculation of creep curves and time-to-rupture diagrams, Materialia. 12 (2020), 100760, https://doi.org/10.1016/j.mtla.2020.100760.

[37] N. Ghoniem, J. Matthews, R. Amodeo, A dislocation model for creep in engineering materials, Res. Mech. 29 (1990) 197–219.

[38] B. Dyson, M. Mclean, Creep deformation of engineering alloys: developments from physical, ISIJ Int. 30 (1990) 802–811, https://doi.org/10.2355/isijinternational.30.802.

[39] M. Basirat, T. Shrestha, G.P. Potirniche, I. Charit, K. Rink, A study of the creep behavior of modified 9Cr–1Mo steel using continuum-damage modeling, Int. J. Plast. 37 (2012) 95–107, https://doi.org/10.1016/j.ijplas.2012.04.004.

[40] E. Orowan, Problems of plastic gliding, Proc. Phys. Soc. 52 (1940) 8–22, https://doi.org/10.1088/0959-5309/52/1/303.

[41] B. Sonderegger, I. Holzer, E. Kozeschnik, C. Sommitsch, Particle distance distributions and their effect on precipitation strengthening, computer methods in materials, Science. 11 (2011) 148–153. https://yadda.icm.edu.pl/yadda/element/bwmeta1.element.baztech-article-BUJ5-0043-0044.

[42] H. Mughrabi, The α-factor in the Taylor flow-stress law in monotonic, cyclic and quasi-stationary deformations: dependence on slip mode, dislocation arrangement and density, Curr. Opin. Solid St. M. 20 (2016) 411–420, https://doi.org/10.1016/j.cossms.2016.07.001.

[43] S.D. Yadav, B. Sonderegger, M. Stracey, C. Poletti, Modelling the creep behaviour of tempered martensitic steel based on a hybrid approach, Mater. Sci. Eng. A 662 (2016) 330–341, https://doi.org/10.1016/j.msea.2016.03.071.

[44] I.M. Lifshitz, V.V. Slyozov, The kinetics of precipitation from supersaturated solid solutions, J. Phys. Chem. Solids 19 (1961) 35–50, https://doi.org/10.1016/0022-3697(61)90054-3.

[45] Z. Wang, O. Muránsky, H. Zhu, T. Wei, A. Sokolova, K. Short, R.N. Wright, On the kinetics of gamma prime (γ') precipitation and its strengthening mechanism in alloy 617 during a long-term thermal aging, Materialia. 11 (2020), 100682, https://doi.org/10.1016/j.mtla.2020.100682.

[46] B. Tippelt, Influence of temperature on microstructural parameters of cyclically deformed nickel single crystals, Philos. Mag. Lett. 74 (1996) 161–166, https://doi.org/10.1080/095008396180317.

[47] C.E. Campbell, A.L. Rukhin, Evaluation of self-diffusion data using weighted means statistics, Acta Mater. 59 (2011) 5194–5201, https://doi.org/10.1016/j.actamat.2011.04.055.

[48] D. Caillard, J. Martin, Dislocation Climb, Thermally Activated Mechanisms in Crystal Plasticity, Pergamon Materials Series, Elsevier Science, Cambrtidge, UK, 2003, pp. 281–319.

[49] J.P. Hirth, J. Lothe, Theory of Dislocations, 2nd edition, John Wiley, New York, 1982, pp. 569–573.

[50] J. Lothe, Theory of dislocation climb in metals, J. Appl. Phys. 31 (1960) 1077–1087, https://doi.org/10.1063/1.1735749.

[51] Special Metals Datasheet on Inconel Alloy 617, no. SMC-029, 2005.

[52] CODATA, The NIST Reference on Constants, Units, and Uncertainty, Online, https://physics.nist.gov/cgi-bin/cuu/Value?k, 2014.

[53] A.S.M.A. Haseeb, Modeling of the effects of athermal flow strength and activation energy for dislocation glide on the nanoindentation creep of nickel thin film at room temperature, Comput. Mater. Sci. 37 (2006) 278–283, https://doi.org/10.1016/j.commatsci.2005.07.006.

[54] Y.M. Wang, A.V. Hamza, E. Ma, Activation volume and density of mobile dislocations in plastically deforming nanocrystalline Ni, Appl. Phys. Lett. 86 (2005), 241917, https://doi.org/10.1063/1.1946899.

[55] Y. Xiao, B. Gan, A.S. Sologubenko, R. Spolenak, J.M. Wheeler, Size- and strain rate-dependence of nickel and Ni–co micropillars with varying stacking fault energy, Mater. Sci. Eng. A 800 (2021), 140266, https://doi.org/10.1016/j.msea.2020.140266.

[56] B. Sonderegger, Modifications of stereological correction methods for precipitate parameters using transmission microscopy, Ultramicroscopy. 106 (2006) 941–950, https://doi.org/10.1016/j.ultramic.2006.04.004.

[57] S. Schröders, S. Sandlöbes, B. Berkels, S. Korte-Kerzel, On the structure of defects in the Fe7Mo6 μ-phase, Acta Mater. 167 (2019) 257–266, https://doi.org/10.1016/j.actamat.2019.01.045.

[58] J. Zhu, H. Je, On the microstructure and its diffraction anomaly of the μ phase in superalloys, Scr. Met. Mater. 24 (1990) 1861–1866, https://doi.org/10.1016/0956-716X(90)90041-E.

[59] H. Jiang, J. Dong, M. Zhang, The characteristics of μ phase precipitated during 720 °C long-term aging in alloy 617B, J. Mater. Res. Technol. 8 (2019) 2461–2465, https://doi.org/10.1016/j.jmrt.2018.11.006.

[60] C. Wert, C. Zener, Interference of growing spherical precipitate particles, J. Appl. Phys. 21 (1950) 5–8, https://doi.org/10.1063/1.1699422.

[61] J. Schubert, Neuauswertung des Zeitstandverhaltens von lösungsgeglühtem Alloy 617 samt seiner Schweißverbindungen im Temperaturbereich 550–1000°C, in: Proc. from FVW/FVHT Conference, 2010, pp. 5–20. Düsseldorf, Germany.

[62] C. Bullough, R. Krein, P. Lombardi, M. Spindler, E. Poggio, Development of an ECCC interim creep rupture datasheet for alloy 617B using a strength averaging and blending approach, in: Proc. 4th Int. ECCC Conf, 2017, pp. 1–11. Düsseldorf, Germany.

[63] W. Ren, R.W. Swindeman, Assessment of Existing Alloy 617 Data for Gen IV Materials Handbook, Technical Report, 2005, https://doi.org/10.2172/1093000. ORNL/TM-2005/510; AF3610300; NEAF265; Online.

[64] V. Knezevic, A. Schneider, C. Landier, Creep behaviour of thick-wall alloy 617 seamless pipes for 700°C power plant technology, Procedia Eng. 55 (2013) 240–245, https://doi.org/10.1016/j.proeng.2013.03.249.

[65] H.E. McCoy, J.F. King, Mechanical Properties of Inconel 617 and 618, Oak Ridge National Laboratory Report, 1985, https://doi.org/10.2172/711763. ORNL/TM-9337; Online.

[66] R. Sandström, J. He, Survey of creep cavitation in fcc metals, in: T. Tanski, W. Borek (Eds.), Study of Grain Boundary Character, IntechOpen, Rijeka, 2017, https://doi.org/10.5772/66592.

[67] J. He, R. Sandström, Application of fundamental models for creep rupture prediction of Sanicro 25 (23Cr25NiWCoCu), Crystals. 9 (2019) 638, https://doi.org/10.3390/cryst9120638.

[68] K. Schmidt, Komponentenverhalten im 700 °C-Kraftwerk- Numerische und experimentelle Untersuchungen, PhD Thesis at MPA Stuttgart, Germany, https://doi.org/10.18419/opus-6436, 2013.

[69] H. Fan, Q. Wang, J.A. El-Awady, D. Raabe, M. Zaiser, Strain rate dependency of dislocation plasticity, Nat. Commun. 12 (2021) 1845, https://doi.org/10.1038/s41467-021-21939-1.

[70] D.M. Owen, T.G. Langdon, Low stress creep behavior: an examination of Nabarro-herring and Harper-Dorn creep, Mater. Sci. Eng. A 216 (1996) 20–29, https://doi.org/10.1016/0921-5093(96)10382-8.

[71] B. Burton, G.L. Reynolds, In defense of diffusional creep, Mater. Sci. Eng. A 191 (1995) 135–141, https://doi.org/10.1016/0921-5093(94)09643-0.

[72] G. Stechauer, E. Kozeschnik, Assessment of substitutional self-diffusion along short-circuit paths in Al, Fe and Ni, Calphad. 47 (2014) 92–99, https://doi.org/10.1016/j.calphad.2014.06.008.

[73] S. Bose, R. Banerjee, A. Genc, P. Raychaudhuri, H.L. Fraser, P. Ayyub, Size induced metal–insulator transition in nanostructured niobium thin films: intra-granular and inter-granular contributions, J. Phys. Condens. Matter 18 (2006) 4553–4566, https://doi.org/10.1088/0953-8984/18/19/010.